

NASA Contractor Report 3629

Heat Generation in Aircraft Tires Under Free Rolling Conditions

Samuel K. Clark and Richard N. Dodge

GRANT NSG-1607
OCTOBER 1982



NASA Contractor Report 3629

Heat Generation in Aircraft Tires Under Free Rolling Conditions

Samuel K. Clark and Richard N. Dodge
University of Michigan
Ann Arbor, Michigan

Prepared for
Langley Research Center
under Grant NSG-1607

NASA
National Aeronautics
and Space Administration

**Scientific and Technical
Information Branch**

1982

INTRODUCTION

The development of heavy transport and military aircraft with high performance characteristics has placed increased demand on landing gear and tire components. Specifically, aircraft tires have developed through the years to a point where the ratio of tire weight to aircraft weight has steadily decreased, due in part to improved tire cord materials, rubber compounds, and tire structural design. However, aircraft tire operations are more demanding wherein the ultimate strength limits of the tire carcass are being approached. Thus, a need exists for the development of methods for predicting the strength limit of aircraft tires on some rational basis other than indoor dynamometer testing.

The problem of tire strength differs from that encountered in the strength of normal metallic structures and the reasons lie in the complexity of the material characteristics of the constituents in an aircraft tire. In an aircraft tire, almost all loads are carried directly by the textile cord reinforcement, commonly nylon as is presently practiced. Some compressive loads are carried by rubber elements in the tread but these are rather minor. In addition to the strength problem, aircraft tires generate substantial temperatures as they roll, both during takeoff and landing. The temperatures are not high in the usual sense of metallic materials, being on the order of hundreds of degrees Fahrenheit or less, but they are high enough to seriously degrade the strength of the load-carrying textile components in the tire. Excessive temperatures can easily cause a tire to fail even if the stress levels are not overly high.

In addition to the interaction of temperature and stress even more complex phenomena are at work in the repeated daily use of aircraft tires. These phenomena are basically associated with the long term strength and adhesion degradation of an aircraft tire due to cyclic variations in stress and temperature. This degradation is an area where not much information is available, and represents a region where the field usage of tires must depend on experience and judgement rather than upon science.

Because of this strength degradation factor, the useful life of aircraft tires is limited, but these limits are not clearly defined and they vary from one aircraft to another and from one user to another.

Substantial advances are being made in the tire industry in calculating stresses imposed on textile cord structures due to load-carrying and inflation pressure. However the area of tire temperature build-up, which is a major cause of tire failure, has been almost untouched and there is no analytical technique suitable for predicting aircraft tire internal temperatures on a rational basis. Hence, the tire designer or manufacturer is not able to compare the anticipated temperature build-up in a new design with previous designs or with known temperature-strength characteristics of the materials which he wishes to use. This void is a serious short-coming in the design process, particularly in the preliminary design of high performance aircraft tires, where a knowledge of anticipated higher temperatures during normal take off and landing cycles would be valuable in assessing the validity of proposed tire, aircraft weight, and ground speed and taxi length combinations.

The present research effort is directed toward construction of a rational method for evaluating internal temperatures of an aircraft tire and for calculating these rapidly and easily, so that the method may be used as a design tool in both the tire and airframe industries.

GEOMETRY OF TIRE DEFORMATION

The basic material property used in the development of the tire heating computational method is the hysteretic loss characteristic of polymeric materials during cyclic stressing. This characteristic is illustrated in figure 1, where a typical stress strain curve for a lossy material is illustrated. As the material is stressed from point A to point B and return, the figure shows that the stress-strain curve of the loading cycle does not coincide with the stress-strain curve of the unloading cycle. The net area under the curve which remains as the material is returned to its original stress state represents a loss of

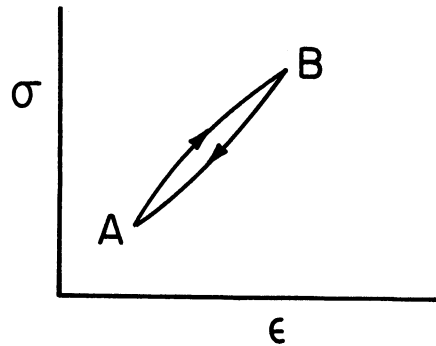


Fig. 1. Typical stress-strain curve of a material illustrating hysteretic loss

mechanical work during the cycle from A to B and return. This lost work is converted into heat and is either diffused through the element and eventually lost from its surfaces or must be accounted for in some way in a heat balance. From the analytical point of view, the work done in a stress cycle as experienced by a material point in passing through the contact patch is expressed most usefully by the use of a simple linear visco-elastic model such as the Kelvin-Voigt solid, and using such a model the energy loss per load cycle may be written as in Equation 1.

$$\Delta E = U \pi \Delta V \cdot \tan \delta \quad (1)$$

where

ΔE = Energy loss/cycle

U = Change in Strain Energy from A to B

$\tan \delta$ = Loss Tangent of Material

ΔV = Volume Element

The question of whether the energy loss depends on the change in strain energy between two non-zero stress points, or upon the difference in strain energy levels each calculated from zero stress level, is treated in Appendix A. It can be demonstrated that the former formulation is the correct one.

This formulation presumes that the initial stress induced by tire inflation has no influence in a linear sense on the energy loss per unit stress cycle. However, the initial stress state may influence the material characteristics, which are not linear in this case. Methods for calculating the change in strain energy will be discussed in the next section of this report.

The method used for calculating the change in strain energy is based on two assumptions. The first is that the tire is made up of a series of material points, each of which undergoes a change in stress state corresponding to the points A and B in figure 1, as it moves from point A to B shown as in figure 2.

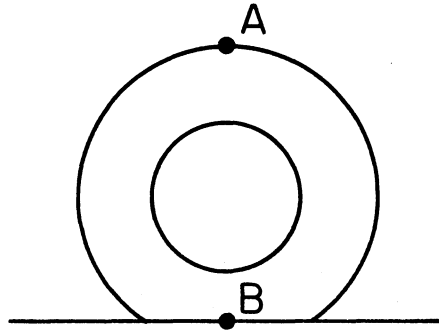


Fig. 2. Extreme points of stress excursion in a tire

As a material point moves from A to B in figure 2, it is assumed that the general wave form of the stress cycle depicted in figure 1 is unimportant, and high harmonics of the cyclic stress are neglected in favor of a single fundamental cyclic stress change, which will be described in terms of an assumed geometry of the tire at point A and B. In other words, no allowance is made in this simplified analysis for a Fourier decomposition of the stress state as the tire moves from A to B, but rather the fundamental harmonic is considered as defining the change in strain energy between the two points.

The second major assumption made in calculating the strain energy of the tire as it rolls through the contact patch is that at both points A and B of fig. 2, the cross-section of the tire may be represented geometrically by its neutral axis, around which act both membrane and bending strains.

The neutral axis of the tire section is usually taken at the mid-thickness location which may be determined approximately by estimation or alternately by calculation. For the case of the inflated tire cross section, the neutral axis may be located by:

- (a) Use of a tire section to approximate the neutral axis, assigning numerical values of co-ordinates to selected points.
- (b) Use of the uninflated tire dimensions and cord angles to provide input data to calculate the inflated tire shape, using such methods as the Hofferberth equation [4], or finite element methods.

In the case of the tires studied in this report, both methods were examined. While the Hofferberth equations are convenient and seem to agree well with measurement in the crown and upper sidewall, they do not agree well in the lower sidewall and bead area where greater bead and rim constraint is present. For that reason the numerical data generated for this report were obtained by approximating the inflated tire cross-section from drawings.

For the deflected tire a similar but more severe situation exists because the deflected cross section must be obtained. Fortunately most aircraft tires are molded in the tread and shoulder regions so that a clear line of demarcation is present between portions in contact with the runway and portions not in contact. This demarcation allows one to assume that the part of the cross section in contact is flat when at the center of the contact patch, as shown in fig. 3. The sidewall portion, out of contact, can then be defined geometrically by a separate calculation. Three possible methods for such a calculation include:

- (a) Some form of finite element solution involving large deformations
- (b) A linearized, energy based deflection analysis of the sidewall arch. The boundary conditions imposed on the sidewall section are:

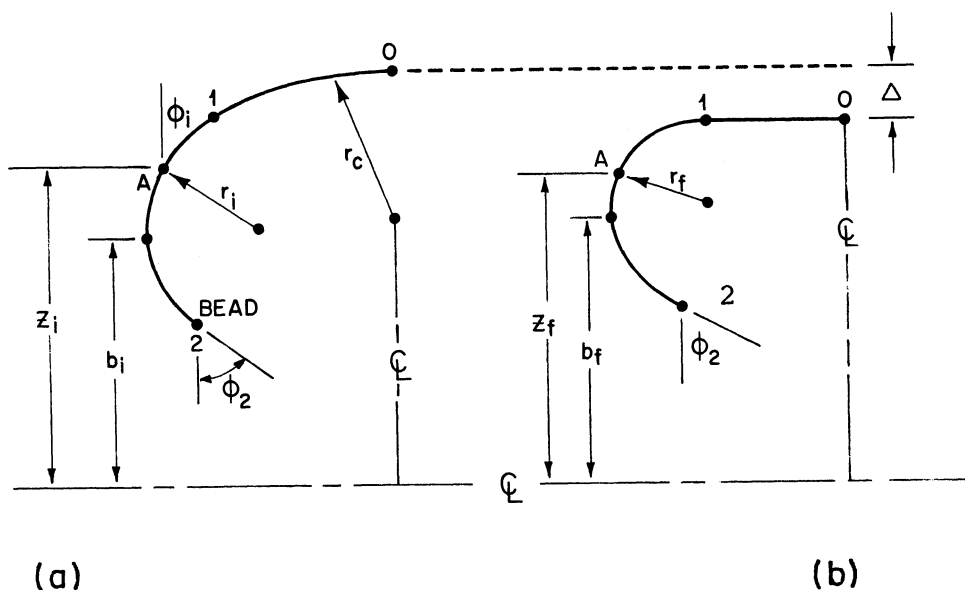
1. At the shoulder the sidewall must have the same deflection as the tread region.

2. At the bead the arch acts as a built-in section with no change in slope.

(c) The assumption that the high pressures commonly used in aircraft tires cause the sidewall to act essentially as a membrane, neglecting bending stiffness. For this assumption, the sidewall may be approximated by using a segment of a circular arc as the sidewall shape.

For simplicity and computational ease the latter method has been used to obtain sidewall shapes. It is surprisingly realistic in spite of its linear approximate character. Tire cross section widths calculated by this method agree well with those observed experimentally.

Figure 3 illustrates the neutral axis of the structural part of the carcass by the lines labeled 0-1-2. The inflated tire geometry is presumed to be represented by fig. 3a. The deformed tire, under deflection Δ as shown in fig. 3b, is presumed to operate under conditions of being perfectly flat



Assumed geometry at point A, Fig 2

Assumed geometry at point B, Fig. 2

Fig. 3

in contact with the runway in section 0-1, and having a reduced radii in the sidewall as given by the symbol r_f . The bead, point 2, is fixed. The regions 0-1 and 1-2 are considered inextensible for computational convenience which allows the complete geometric description of the various radii of curvature, once the tire deflection Δ and the initial tire geometry are given under inflated conditions. The computational details of the geometric representation are given in Appendix B.

A material point is subject to both bending and membrane strain during deformation of the tire from point A to point B as shown in fig. 2. The bending strains are dependent on the radius of curvature of the tire carcass midline as illustrated in fig. 3, as well as upon the distance measured perpendicular from this carcass midline. The bending strain can be calculated in the usual linear elastic fashion based upon a knowledge of change in radius of curvature of the carcass midline between the two points in question in fig. 2.

Membrane strains also exist in the tire cross section due to the high inflation pressure commonly used in aircraft tires. Some of these membrane strains are not directly obtainable from the geometric changes which have been postulated, since they depend heavily on contact patch boundary conditions. Other membrane strains must be obtained from a knowledge of the membrane stresses in the tire. These membrane stresses in turn depend upon the curvature characteristics of the tire, as well as upon certain geometric variables which may be calculated from the tire cross section geometries given in fig. 3. The details of these calculations are given in Appendix B. In particular, the sidewall area must be carefully defined since the point of vertical tangency of the tire is an important factor in computation of membrane stresses. This point of vertical tangency, measured as the distance b in fig. 3, shifts during the deformation process, and the position of the various material points relative to this point of vertical tangency must be tracked in the subsequent computations.

Since aircraft tire deflections are normally large, a further assumption is made that the tire deformation process causes changes in the tire cross section, such as shown in fig. 3, but that deformations in the circumferential direction are negligible.

It is also necessary to track the radius of a material point from the axis of rotation of the wheel during the deformation process, as shown in fig. 4. The variable used for such measurement is denoted by the symbol z . In fig. 4, the point j represents a material point which changes its axisymmetric radius during the deformation process as the wheel rotates from condition A to condition B. The details of the computation of such a change are also given in Appendix B.

Bead tensions also change during the deformation process and must be incorporated into a cyclic stress mechanism involving a loss characteristic of the bead itself. These bead

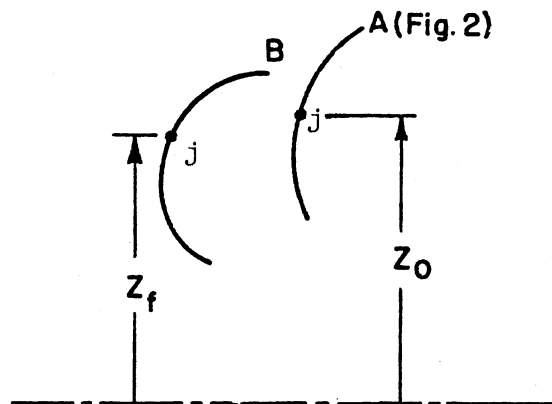


Fig. 4. Tire cross sections

tensions depend on angle of tangency of the side wall at the bead, denoted as point 2 in fig. 3. Computations of bead tension are given in Appendix C where the bead geometry and assumptions governing it are discussed in more detail.

TIRE DEFORMATION AND STRESS

For the calculation of the strain energy change during the rotation of a material point through the contact patch we rely heavily on the assumed tire deformation given in figures 2 through 4.

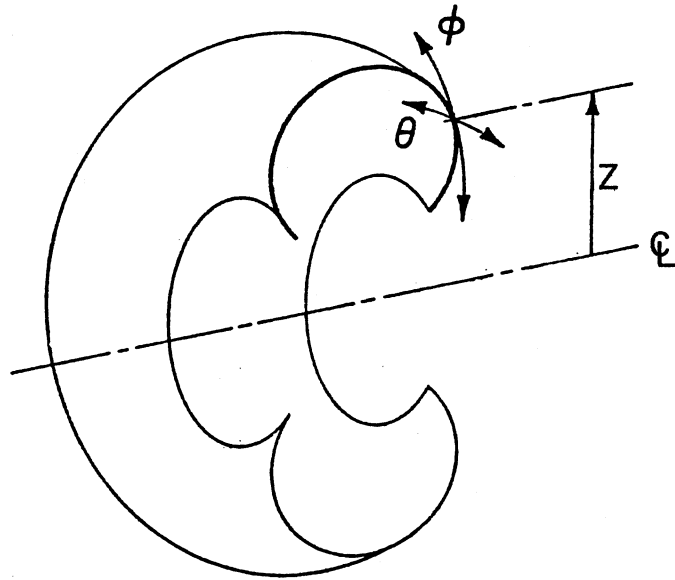


Fig. 5. Tire coordinate notation

Fig. 5 illustrates the geometry involved and the notation being used here. z represents radial distance from the axis of rotation of the tire, ϕ represents the meridional direction and θ represents circumferential direction.

For purposes of computing changes in strain energy states during the cyclic loading process the tire is divided into five regions, denoted as I-V in fig. 6.

The rationale behind the division of the tire into these parts is that region II represents the tread region of the tire, which is considered to be rubber-like and in contact with the runway surface. It is usually characterized by material isotropy

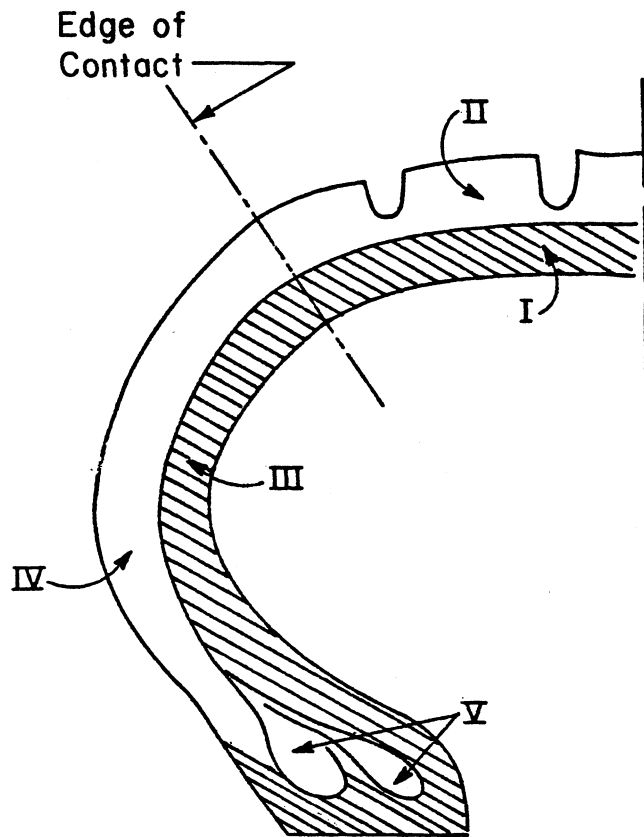


Fig. 6. Tire cross section showing regions of different characteristic and loading patterns

and by an elastic shear modulus which is nearly linear up to reasonably large strains. Further, it exhibits near incompressibility, and that fact is used in computing the strain state associated with contact against the runway surface.

The region denoted by I is immediately beneath the tread region of the tire and is firmly affixed to it, so that the membrane strain state of the two elements is considered to be the same. However, region I is assumed to be plane orthotropic in its characteristics, and may be thought of as a sheet of material lying in the ϕ - θ plane as illustrated in fig. 7.

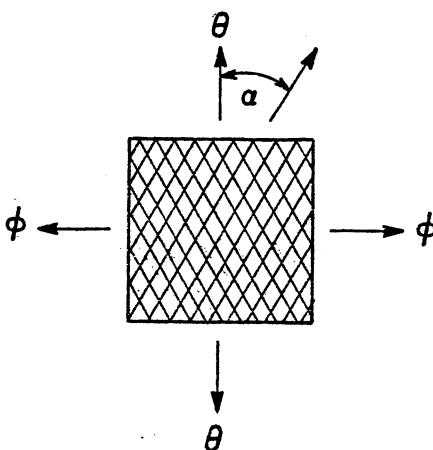


Fig. 7. Laminate characteristics in Region I

In fig. 7 the diagonal lines represent textile reinforcing cords, which serve to give the primary stiffness to the carcass region. Because of their diagonal character, which is typical of a bias aircraft tire, the element shown in fig. 7 will exhibit different elastic constants in the ϕ and θ directions. Such materials have been studied in the tire industry and their characteristics can be estimated. Reference [6] gives a detailed derivation of the appropriate elastic constants for a plane orthotropic material using the structure shown in fig 7, adequate to within a range of diagonal reinforcing angles α encountered in aircraft tire construction. Fig. 7 can be characterized in terms of elastic constants dependent upon the rubber and cord reinforcing materials and upon the half-angle α illustrated in the figure.

Regions III and IV of the tire, as illustrated in fig 6, represent the sidewall areas which also are subjected to changes of curvature as the tire deforms. These areas do not contact the runway surface, so that in Region III the carcass strains are again determined and the elastic constants obtained from the model of fig. 7. These constants are utilized to determine the

appropriate strain energy expressions. Region IV represents a rubber covering used primarily as a scuff or abrasion resistant coating on the outside of the tire. It contributes to tire mechanical loss and to the subsequent heat build up, but is not structural in nature. The assumption is made that this covering is bonded tightly to the carcass of Region III and undergoes the same membrane strains as those of Region III, but, in addition, undergoes bending strains due to its distance away from the neutral axis, which because of the relatively high textile modulus is usually located in Region III of the carcass.

Region V is the tire bead. It requires a separate analysis, not only because of the force fluctuations in the beads but also because the beads are conventionally made of rubber coated steel wire which has significantly different elastic and loss characteristics than the remainder of the tire.

For computational purposes the calculation of strain energy stored in the tire during the deformation process is accomplished by means of splitting each region of the tire into a number of cells, each cell being denoted by a pair of numbers in matrix notation fashion. The element numbering system for the cells in the tire cross-section is illustrated in figure 8. The elements shown in this figure are purely for illustration purposes. Any number of elements may be chosen and the order of them may be adjusted to suit the needs of the user, but for the instances to be illustrated here numbering begins in the bead area and terminates at the center line of the tire crown. Numbering of the vertical location of the elements begins at the inner surface and terminates at the tread or outer surface of the tire.

The inner liner of the tire, while pure rubber, is thin enough so that it may be included with the composite carcass material.

Computation with the individual elements is facilitated by use of the matrix notation illustrated in figure 8. However, for a general theoretical treatment of the strain energy change in the tire in this report the notation of figure 6 is adopted, where the major portions of the tire are delineated. An approximate analysis of the strain energy in each of the Regions I-V of the tire is now given.

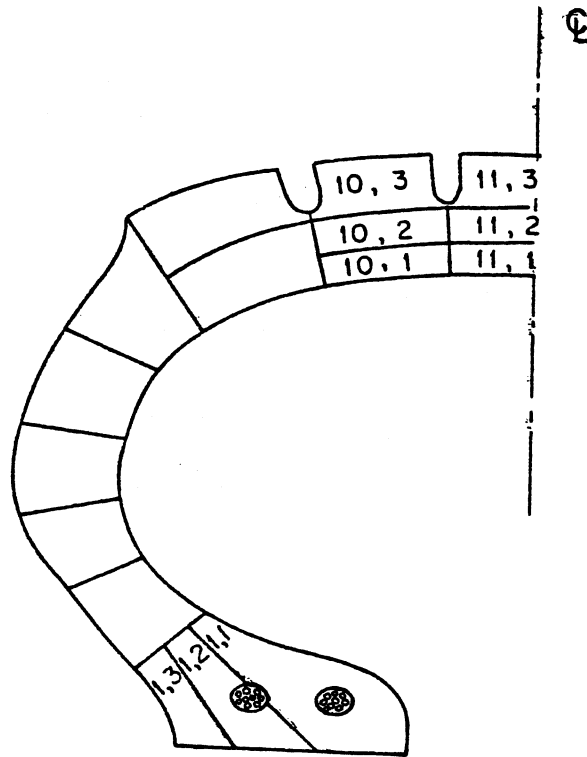


Fig. 8. Element numbering system

Region I

In this section the assumed geometry of figure 3 is used to develop membrane stresses in the ϕ (meridional) direction. A shear effect is included and will be discussed later.

(a) Undeformed Position

First consider the tire in the undeflected position (point A of fig. 3). Referring to figs. 3, 4, and 9, equilibrium of the axisymmetric annular shell element o-s gives a membrane stress

$$\sigma_{\phi_m} = \frac{P_o}{2h} \frac{(z_s^2 - b^2)}{z_s \sin \phi_s} \quad (2)$$

Assuming that changes in shape from the uninflated to the inflated state are small, the bending stresses here are negligible so that

$$\sigma_{\phi_b} \approx 0. \quad (3)$$

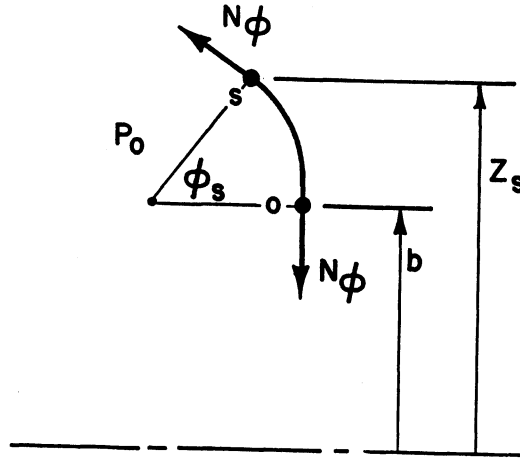


Fig. 9. Membrane force nomenclature

The membrane stresses in the θ direction are obtained from the nature of the load carrying cord network shown in fig. 7. It may be demonstrated that in a soft matrix where the cords carry the entire load,

$$\sigma_{\theta_m} = \sigma_{\phi_m} \cdot \cot^2 \alpha \quad (4)$$

where α is the cord half-angle shown in fig. 7. The cord angle relation is discussed in more detail in Appendix D. The θ directed bending stresses are also assumed to vanish so that, similar to equation (3)

$$\sigma_{\theta_b} \approx 0 \quad (5)$$

The total stress state in the undeformed but inflated condition, point A of fig. 10, is given by the membrane stresses just determined. It is denoted by the subscript 'A', taken from Fig. 10.

$$(\sigma_{\phi})_A = \sigma_{\phi,m} \quad \text{Ref. equation (2)}$$

$$(\sigma_{\theta})_A = \sigma_{\theta,m} \quad \text{Ref. equation (4)}$$

(b) Deformed Position

Eq. (2) gives the meridional membrane stress σ_{ϕ_m} in terms of the sidewall geometry of the tire. In the previous sections it was shown how sidewall geometry may be determined in the deformed position. Assuming that it is available, then σ_{ϕ_m} may be found at the points labeled C and E in fig. 11, i.e. the edges of the contact patch. Denote this by $\sigma_{\phi,m}^*$

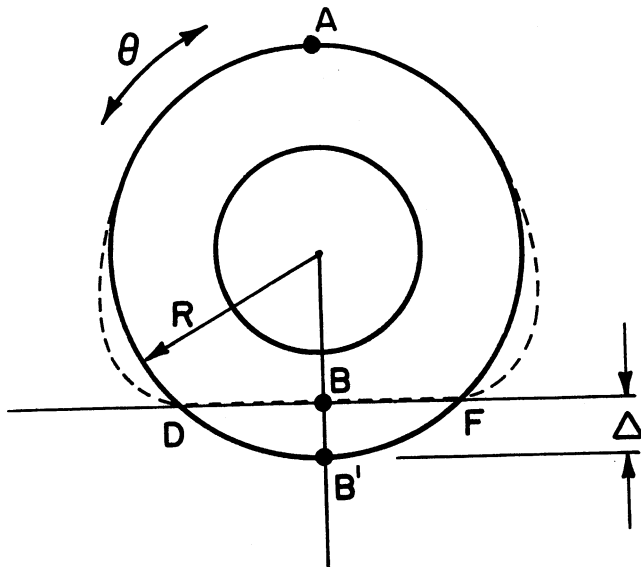


Fig. 10. Side view of tire

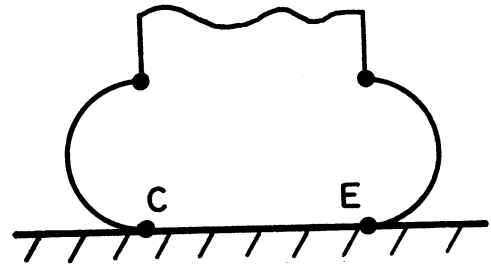


Fig. 11. Section through B-B' of Fig. 10

The entire contact patch region C-D-E-F of figs. 10 and 11 is assumed to be flat and in contact with the runway. Were it not for friction between tire and runway, the flat contact patch region would be subjected to a constant membrane stress value across its width of

$$\sigma_{\phi,m} = \sigma_{\phi,m}^* \quad (6a)$$

where $\sigma_{\phi,m}^*$ is the value of the membrane stress at the edge of contact, points C and E of fig. 11.

Due to the presence of frictional effects the stress $\sigma_{\phi,m}$ cannot decay fully to the value given by equation (6a), but instead a correction factor must be placed on the stress difference depending on position inside the contact patch. This analysis is given in Appendix K, and the appropriate factors are included in the numerical computations which follow.

The circumferential membrane stress σ_{θ} may once again be determined from the relation originally given in equation 4.

$$\sigma_{\theta,m} = \sigma_{\phi,m}^* \cot^2 \alpha \quad (6b)$$

With this relation, the membrane stress state may be determined in the deformed position of Region I. This stress must also be corrected by the same friction effect.

In addition to these membrane stresses, bending effects are present in the contact region of the tire since the carcass is flat when it is in contact with the runway surface. The curvature changes undergone by the carcass are assumed to be exactly equal to the reciprocals of the principal radii of curvature of the tire, namely the values R of Fig. 10 and r_c of Fig. 3. Using these values, the bending strains may be determined as

$$\epsilon_{\phi,b} = (\bar{y}-y) \left(\frac{1}{r_c} \right) \quad \epsilon_{\theta} = (\bar{y}-y) \left(\frac{1}{R} + \frac{2}{D} \right)$$

where y is measured from the inside surface positive toward the outer surface of the tire. Note that when running on a drum this curvature can be included by defining the curvature change in the θ direction as $(1/R+2/D)$, where D is the drum diameter.

These strains may be used in conjunction with the usual orthotropic stress-strain relations commonly applied to bias cord-rubber constructions to obtain the stresses associated with bending. These become

$$\sigma_{\phi,b} = \frac{E_{\phi}}{1-\mu_{\phi\theta}\mu_{\theta\phi}} [\epsilon_{\phi,b} + \mu_{\phi\theta}\epsilon_{\theta,b}] \quad (7)$$

$$\sigma_{\theta,b} = \frac{E_{\theta}}{1-\mu_{\phi\theta}\mu_{\theta\phi}} [\epsilon_{\theta,b} + \mu_{\theta\phi}\epsilon_{\phi,b}] \quad (8)$$

The total stresses are now given by the sum of the bending terms equations (7) and (8) added to the membrane stress terms of equation (6). Again, the subscript 'B' is from fig. 10 to denote the deformed condition

$$(\sigma_{\phi})_B = \sigma_{\phi,m} + \sigma_{\phi,b} \quad (9)$$

$$(\sigma_{\theta})_B = \sigma_{\theta,m} + \sigma_{\theta,b}$$

The strain energy density is now based on the stress differences which take place between points A and B of fig. 10 and which were illustrated earlier in fig. 1.

In order to form this strain energy density the stress difference or change from A to B is first formed. This stress change is then used to determine the strain change accompanying it. These changes then can be combined to form the change in strain energy from the A to B conditions. Denoting changes by the symbol Δ , one finds

$$\Delta\sigma_{\phi} = (\sigma_{\phi})_B - (\sigma_{\phi})_A \quad (10)$$

$$\Delta\sigma_{\theta} = (\sigma_{\theta})_B - (\sigma_{\theta})_A$$

Using orthotropic elastic properties,

$$\Delta\epsilon_{\phi} = \frac{\Delta\sigma_{\phi}}{E_{\phi}} - \mu_{\phi\theta} \frac{\Delta\sigma_{\theta}}{E_{\theta}}$$

$$\Delta \epsilon_{\theta} = \frac{\Delta \sigma_{\theta}}{E_{\theta}} - \mu_{\theta\phi} \frac{\Delta \sigma_{\phi}}{E_{\phi}} \quad (11)$$

The strain energy density is now given by

$$U_c = \frac{1}{2}(\Delta \sigma_{\phi} \Delta \epsilon_{\phi} + \Delta \sigma_{\theta} \Delta \epsilon_{\theta}) \quad (12)$$

The elastic constants needed for these formulations of strain energy are derived in Appendix E.

The other contribution to strain energy in Region I is caused by the change in the membrane stress state as the tire rolls through the contact patch region. These changing tensile stresses result in shear in the sidewall and contact area. This analysis is rather lengthy but leads to contributions which can be significant, particularly for larger tires. The details of this analysis are also presented in Appendix E. The resulting strain energy density is given in summary form

$$U_s = \left[\frac{0.858 \{ (\sigma_{\phi,m})_A - (\sigma_{\phi,m})_B \} \int_0^S \cot^2 \alpha ds}{\{ 3\Delta(D-\Delta) \}} \right]^2 \cdot \frac{1}{2G_{\phi\theta}}$$

where the symbols used are defined in Appendices E and F.

Because of the complications arising from introduction of anisotropic elastic constants, these two strain energy densities will be summed algebraically in order to give the total strain energy

$$U = U_c + U_s \quad (14)$$

for Region I.

Region II

The basic assumption used in calculating the strain energy in the tread rubber is that this material is non-structural, and that it undergoes the same membrane strain as the carcass immediately underneath to which it is bonded. Its bending strain is determined by its distance from the neutral axis and by the Kirchoff hypothesis.

(a) Undeformed Position

The carcass membrane stresses in the undeformed position have been determined in equations (2) and (4). These stresses can be

used along with the conventional orthotropic stress-strain relations to obtain the membrane strains in that position

$$\begin{aligned} (\epsilon_{\phi})_A &= (\epsilon_{\phi,m})_A = \frac{(\sigma_{\phi})_A}{E_{\phi}} - \mu_{\phi\theta} \frac{(\sigma_{\theta})_A}{E_{\theta}} \\ (\epsilon_{\theta})_A &= (\epsilon_{\theta,m})_A = \frac{(\sigma_{\theta})_A}{E_{\theta}} - \mu_{\theta\phi} \frac{(\sigma_{\phi})_A}{E_{\phi}} \end{aligned} \quad (15)$$

(b) Deformed Position

Similarly, the membrane stresses in the deformed carcass were found in Eqs. (6a) and (6b), from which the corresponding strains are found to be

$$\begin{aligned} \epsilon_{\phi,m} &= \frac{\sigma_{\phi,m}^*}{E_{\phi}} - \mu_{\phi\theta} \frac{\sigma_{\theta,m}^*}{E_{\theta}} \\ \epsilon_{\theta,m} &= \frac{\sigma_{\theta,m}^*}{E_{\theta}} - \mu_{\theta\phi} \frac{\sigma_{\phi,m}^*}{E_{\phi}} \end{aligned} \quad (16)$$

In addition the deformed state also exhibits bending strains. Due to different distances from the neutral axis, these are now dependent on local element geometry. In general the bending strains may be expressed as

$$\begin{aligned} \epsilon_{\phi,b} &= (\bar{y}-y) \cdot \frac{1}{r_c} \\ \epsilon_{\theta,b} &= (\bar{y}-y) \left(\frac{1}{R} + \frac{2}{D} \right) \end{aligned} \quad (17)$$

The total strains are now given for the deformed position by

$$\begin{aligned} (\epsilon_{\phi})_B &= (\epsilon_{\phi,m}) + (\epsilon_{\phi,b}) \\ (\epsilon_{\theta})_B &= (\epsilon_{\theta,m}) + (\epsilon_{\theta,b}) \end{aligned} \quad (18)$$

The changes in strain between the undeformed 'A' position and the deformed 'B' position are taken to be principal strains.

$$\begin{aligned}\Delta\epsilon_{\phi} &= (\epsilon_{\phi})_B - (\epsilon_{\phi})_A \\ \Delta\epsilon_{\theta} &= (\epsilon_{\theta})_B - (\epsilon_{\theta})_A\end{aligned}\tag{19}$$

These strains are caused by deformation of the tire carcass and result in stress changes given by

$$\begin{aligned}\Delta\sigma_{\phi} &= \frac{E_r}{1-\mu}(\Delta\epsilon_{\phi} + \mu\Delta\epsilon_{\theta}) \\ \Delta\sigma_{\theta} &= \frac{E_r}{1-\mu}(\Delta\epsilon_{\theta} + \mu\Delta\epsilon_{\phi})\end{aligned}$$

where E_r and μ refer to isotropic elastic constants of the tread rubber. Thus strain energy can be expressed in the form

$$U_T = 2G[\Delta\epsilon_{\phi}^2 + \Delta\epsilon_{\theta}^2 + \Delta\epsilon_{\phi}\Delta\epsilon_{\theta}]\tag{20}$$

The maximum value of the compressive contact stress results in compressive strains in the approximate value of

$$\epsilon_z = \frac{1.875 P_o}{E_r}$$

where the rationale for the use of the numerical value 1.875 is given in Appendix G where p_o is the tire inflation pressure and E_r the Young's modulus of the tread rubber.

In spite of the incompressible nature of the tread rubber all three principal strains $\Delta\epsilon_{\phi}$, $\Delta\epsilon_{\theta}$ and ϵ_z can exist since the groove pattern molded into the tread allows bulging of the individual tread ribs independent of the ϕ and θ strains.

The additional strain energy caused by the contact pressure is given by

$$U_z = \frac{1}{2} \frac{(1.875 P_o)^2}{E_r} \quad (21)$$

The total strain energy change is now given by the sum of equations (20) and (21)

$$\begin{aligned} U &= U_T + U_z \\ &= 2G[\Delta\epsilon_\theta^2 + \Delta\epsilon_\phi^2 + \Delta\epsilon_\phi \Delta\epsilon_\theta] + \frac{1}{2} \cdot \frac{(1.875 P_o)^2}{E_r} \end{aligned}$$

Region III

(a) Undeformed Position

In this region the analysis of strain energy density is very similar to that of Region I. In the inflated state, as shown at point A of fig. 10, the membrane stress in the meridional direction ϕ is given once more by equation (2)

$$(\sigma_\phi)_A = \sigma_{\phi,m} = \frac{P_o}{2h} \frac{(z^2 - b^2)}{z \sin \phi}$$

and the circumferential stress by equation (4)

$$(\sigma_\theta)_A = \sigma_{\theta,m} = \sigma_{\phi,m} \cot^2 \alpha$$

Again, bending stresses in both ϕ and θ directions are considered negligible.

(b) Deformed Position

In the deformed position the membrane stresses are still governed by equilibrium considerations such as given by equations (2) and (4), but now with use of the deformed geometry appropriate to the center of the contact patch such as point B of fig. 10. This computation still relies on the assumed axisymmetric character of the stress, so that the tire acts as if it were inflated in a barrel. The new sidewall positions must be calculated based on the deformed sidewall geometry as discussed earlier. Using

this assumed geometry, then the deformed position stresses become

$$\sigma_{\phi,m} = \frac{P_o}{2h} \frac{(\bar{z}^2 - \bar{b}^2)}{\bar{z} \sin \bar{\phi}} \quad (22)$$

$$\sigma_{\theta,m} = \sigma_{\phi,m} \cot^2 \alpha$$

where the symbols \bar{z} , \bar{b} , $\bar{\phi}$ denote those quantities measured in the deformed position.

Bending strains are also present in the ϕ direction due to the large changes in radius of curvature which are imposed on the tire sidewall. Curvature changes in the θ direction are neglected leading to a strain change

$$\Delta \epsilon_{\phi,b} = (y - \bar{y}) \left(\frac{1}{r_f} - \frac{1}{r_i} \right) \quad (23)$$

where r_f , r_i = radii of curvature in the meridian plane, final and initial respectively.

Using Hooke's law for an orthotropic material, the bending stresses generated by this bending strain are

$$\sigma_{\phi,b} = \frac{E_{\phi}}{1 - \mu_{\phi\theta} \mu_{\theta\phi}} \Delta \epsilon_{\phi,b} \quad (24)$$

$$\sigma_{\theta,b} = \frac{\mu_{\theta\phi} E_{\theta}}{1 - \mu_{\theta\phi} \mu_{\phi\theta}} \Delta \epsilon_{\phi,b}$$

The total stresses in the deformed state are

$$(\sigma_{\phi})_B = \sigma_{\phi,m} + \sigma_{\phi,b} \quad (25)$$

$$(\sigma_{\theta})_B = \sigma_{\theta,m} + \sigma_{\theta,b}$$

and the stress excursion from position A to position B is

$$\Delta\sigma_{\phi} = (\sigma_{\phi})_B - (\sigma_{\phi})_A \quad (26)$$

$$\Delta\sigma_{\theta} = (\sigma_{\theta})_B - (\sigma_{\theta})_A$$

This stress change causes a strain change

$$\Delta\epsilon_{\phi} = \frac{\Delta\sigma_{\phi}}{E_{\phi}} - \mu_{\phi\theta} \frac{\Delta\sigma_{\theta}}{E_{\theta}} \quad (27)$$

$$\Delta\epsilon_{\theta} = \frac{\Delta\sigma_{\theta}}{E_{\theta}} - \mu_{\theta\phi} \frac{\Delta\sigma_{\phi}}{E_{\phi}}$$

These changes can be used to form the strain energy

$$U_C = \frac{1}{2}(\Delta\sigma_{\phi}\Delta\epsilon_{\phi} + \Delta\sigma_{\theta}\Delta\epsilon_{\theta}) \quad (28)$$

The shear forces previously discussed are also present in the sidewall, and these should also be included here as given in Eq. (13), so that the total strain energy is given by

$$U = U_C + U_S$$

Region IV

Here the same approach is taken as in the previous Region III where the total sidewall strain change is calculated using both the membrane effects and the bending induced by the curvature changes. These strains are given by equation (28). Using this equation and knowing the isotropic character of the rubber covering on the sidewall and shoulder area not in contact with the runway surface, then

$$U = 2G(\Delta\epsilon_{\phi}^2 + \Delta\epsilon_{\theta}^2 + \Delta\epsilon_{\theta} \cdot \Delta\epsilon_{\phi}) \quad (29)$$

as in equation (20). Shear deformation is neglected here.

Region V

In this region the bead elements themselves are considered as components which lose energy during cyclic stressing of the tire. An analysis of this is given in Appendix C, and the result of that analysis may be used to introduce a total or gross strain energy change in each bead of the tire. Using the expressions derived in Appendix C, the energy change becomes

$$U = \frac{1}{2}(T_f - T_i)^2 / A_B^2 E_B \quad (30)$$

where T_f = final bead tension
 T_i = initial bead tension
 A_B = bead cross sectional area
 E_B = bead modulus

HEAT GENERATION RATES

For purposes of obtaining heat generation rates from strain energy stored during elastic cycling of the tire, the conventional Kelvin-Voigt mechanical model of an elastic solid is utilized which exhibits loss characteristics under cyclic stress. Figure 1 can represent experimental data observed on many materials, including the polymeric materials used in aircraft tires such as rubber, nylon in textile cord form, and even the bead wire assembly, provided that the loss characteristics are measured properly. One widely accepted method of representing such a phenomena, the Kelvin-Voigt model, is illustrated in fig. 12 using the conventional spring and dashpot notation.

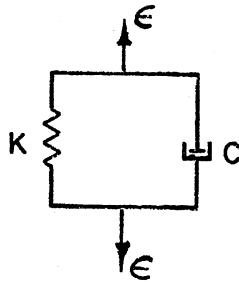


Fig. 12. Spring-dashpot model of a material exhibiting loss

Imposing a cyclic sinusoidal strain in the form

$$\epsilon = \epsilon_0 \sin \omega t, \quad (31)$$

the stress necessary to maintain such a sinusoidal strain is given by

$$\sigma = K\epsilon + C\dot{\epsilon} = K\epsilon_0 \sin \omega t + C\omega\epsilon_0 \cos \omega t \quad (32)$$

It is customary to convert this representation into a form using the elastic constants E' and E'' , which represent the characteristics of a material exhibiting loss, as follows

$$\sigma = E' \epsilon_o \sin \omega t + E'' \epsilon_o \cos \omega t \quad (33)$$

It is clear from this representation that both E' and E'' may be, and usually are, functions of frequency. In addition, particularly in polymeric materials, they show marked dependence on temperature and, of course, on material composition.

The energy loss during one cycle of stress is given by

$$\text{Energy Loss} = W = \int_{\text{half-cycle}} \sigma d\epsilon = \frac{\pi E'' \epsilon_o^2}{2} \quad (34)$$

Defining the ratio of E'' to E' as follows

$$E''/E' = \tan \delta \quad (35)$$

and combining equations 33 and 34 gives

$$W = \pi \frac{E' \epsilon_o^2}{2} \tan \delta = \pi U \tan \delta \quad (36)$$

where U is the change in elastic strain energy during the cyclic stressing process. Equation 36 is in the form in which energy loss is commonly expressed, using the elastic constants E' and E'' directly obtained from experimental data, or, alternately, using $\tan \delta$ directly obtained from measurement. Several instruments are commercially available for the measurement of loss properties such as $\tan \delta$, and values of $\tan \delta$ are available for many polymeric materials.

The energy lost in going from one stress state to another is represented by using the change in stress or in strain when computing the strain energy term U in equation (36). This energy loss has been discussed and is demonstrated experimentally in Appendix A.

The units of Eq. 36 are the same as those of strain energy, namely work per unit volume. However, these units must be converted to a rate of heat generation per unit volume in order to be used in the general heat diffusion equation discussed in the subsequent sections. Since aircraft velocities are commonly expressed in English units of feet per second, $\tan \delta$ is dimensionless, and the tire diameter may conveniently be expressed in inches, and using the elastic strain energy in inch/pound units, then one may write:

$$\begin{aligned} U/12 &= \frac{\text{ft. lbs. energy}}{\text{cu. in. volume}} / \text{stress cycle} \\ &\times \frac{1}{778} \text{ BTU/in}^3 / \text{cycle} \\ &\times 252 \text{ cal/in}^3 / \text{cycle} \\ &\times \frac{1}{(2.54)^3} \text{ cal/cm}^3 / \text{cycle} \end{aligned}$$

$$\text{But } \frac{r_r \omega}{12} = v_o$$

where v_o = aircraft velocity, fps

r_r = rolling radius of tire, inches

$$\approx r_o - \Delta/3$$

ω = tire angular velocity, rad/sec

$$= \frac{12v_o}{(r_o - \Delta/3)} \times \frac{1}{2\pi} \text{ cycles/sec.}$$

$$\text{Loss/cycle} = W = \pi U \tan \delta$$

Heat generation rate \dot{q} in $\text{cal/cm}^3/\text{sec}$ may be expressed as follows

$$\begin{aligned} \dot{q} &= U \times \frac{1}{12} \times \frac{252}{778} \times \left(\frac{1}{2.54}\right)^3 \times \frac{12}{2\pi} \times \frac{v_o}{(r_o - \Delta/3)} \times \pi \tan \delta \\ &= .00988 \frac{U v_o \tan \delta}{(r_o - \Delta/3)} \approx 0.01 \frac{U v_o \tan \delta}{(r_o - \Delta/3)} \end{aligned} \quad (37)$$

where r_o = outside radius of tire, inches.

Δ = tire deflection, inches

v_o = aircraft velocity, feet/second

U = elastic energy, inch-pounds/cubic inch, stored
due to the change in stress state.

TEMPERATURE DISTRIBUTION MODEL

Referring first to fig. 8, the tire must be divided into segments or cells wherein in each the rate of heat generation is considered constant, and the temperature can be calculated on the basis of being averaged across the cell area. In assigning the geometric location of cells such as illustrated in fig. 8, material constancy is maintained across each cell, in the sense that the interface between the pure rubber region and the carcass region is used as a dividing line for a series of cells. This procedure allows the properties of each cell to be essentially uniform, which is a considerable convenience in subsequent calculations. The stress state in each cell is calculated on the basis of the centroid of each cell area, and is considered to be averaged across the cell volume. The geometric location of the cell is taken to be the coordinates of the cell centroid of area such as shown in fig. 13.

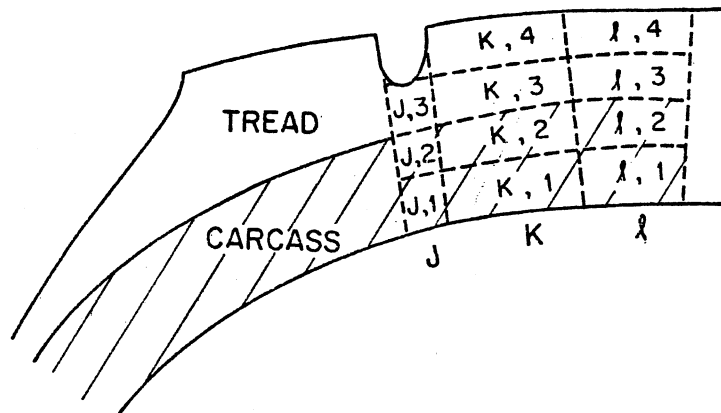


Fig. 13. Distribution of computational elements in the tread region

Quadrilateral elements have been consistently utilized in constructing the numerical analog to this solution. Thus each element either loses or gains heat from four faces, and this exchange may be through conduction when the element in question is bounded by a similar element or it may be by convection from a surface face, or it may be by conduction to either the flange of the wheel or to the runway surface for those special elements which come in contact with them.

For purposes of conduction to the wheel flange, a similar set of elements to those shown in fig. 13 must be laid out on the wheel flange using the appropriate thermal characteristics of the wheel material, so that heat flow can take place by direct conduction between the bead area of the tire and the flange. There will inevitably be a certain contact resistance between the bead seat and the flange material, but this factor is as yet unknown and is neglected in the subsequent computations.

Contact with the runway surface is more difficult to quantify since it occurs only periodically. To a first approximation that process is treated in a similar fashion using the thermal conductivity of the runway material, but allowing only that fraction of the conduction process to occur as is proportional to the time spent by each surface element in contact with the runway. The remaining part of the cycle is occupied by those tread surface elements which contacted the runway surface now freely moving in the atmosphere, and during that fraction of the cycle the normal convection process from the surface occurs.

Using the well known expression for diffusion of heat in a solid body under conditions of internal heat generation, such as given by Carslaw and Jaeger [1], the equation for conduction of heat for a typical element is given by

$$K \nabla^2 \theta = \rho \frac{\partial \theta}{\partial t} - \dot{q} \quad (38)$$

This expression may be written for finite difference purposes in the form

$$\frac{\Delta \theta}{\Delta t} = \dot{q} + \bar{\alpha}_{K-1,K,\ell} (\theta_{K-1,\ell} - \theta_{K,\ell}) + \bar{\alpha}_{K,K+1,\ell} (\theta_{K+1,\ell} - \theta_{K,\ell})$$

$$+ \bar{\alpha}_{K, \ell-1, \ell} (\theta_{K, \ell-1} - \theta_{K, \ell}) + \bar{\alpha}_{K, \ell, \ell+1} (\theta_{K, \ell+1} - \theta_{K, \ell}) \quad (39)$$

where the elements used in equation 39 are illustrated in fig. 14, and where

$$\bar{\alpha}_{m, n} = \frac{KA}{d}$$

with

K = thermal conductivity

A = area of contact between subscripted elements

d = distance between centroids of subscripted elements

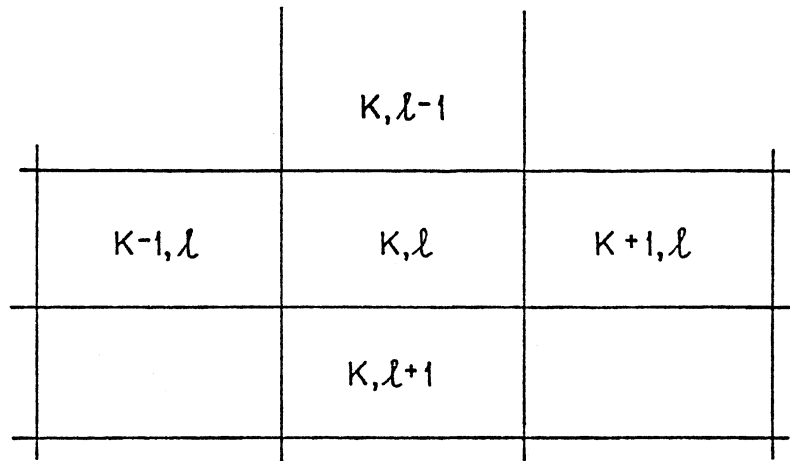


Fig. 14. Notation for thermal elements

The basic method of computation is to use small time increments and to calculate the temperature rise in each cell utilizing the temperatures of adjoining elements from the previous time increment computation. There are several factors which make this type of computation possible. First of all, it is well known in heat transfer calculations that if the quantity given by the expression

$$M = \frac{\Delta x^2}{a \Delta t} \quad (40)$$

where

$$\begin{aligned} a &= \dot{q}/\alpha \\ \Delta x &= \text{element size} \\ \Delta t &= \text{time increment} \end{aligned}$$

is large, then stability of such a time based forward computation is assured and convergence to correct results will be obtained. For that reason cell elements have been kept moderately large and time increments small since this reduces requirements for computer memory and also insures stability of the computation. Secondly, the dominant term is the rate of heat generation \dot{q} , and for purposes for aircraft taxi and take-off the heat build up occurs over a relatively short period of time, so that the heat generation term almost completely controls the temperature rise in the tire. Heat diffusion, at least for the take-off case, is a minimal effect. Thus, heat conduction using adjoining cell temperatures from the previous time interval incurs only very small errors in the final temperature distribution in the tire.

The heat transfer coefficients from tire to air are not particularly well known in this case, but again it is fortunate that taxi take-off cycles are relatively short, so that again the rate of internal heat generation is the dominant term. However, in studying taxi and combined taxi take-off operations, more emphasis is placed on the accuracy of the heat transfer and heat conduction coefficients associated with this problem. In that case those coefficients become more important. The numerical proportioning of the heat transfer coefficients is given in detail in Appendix H.

The method of temperature computation using Eq. 39 now consists of starting from whatever initial temperature state one wishes in each of the cells, allowing a short time interval to take place and computing the heat generated in each cell using

the concepts developed in the previous two sections. In carrying out such computations a knowledge of the material loss characteristic, $\tan\delta$, must be known, and these are given in the last section of this report.

At the end of the first time interval the temperature field in the entire tire is calculated and is used as a basis for the heat transfer characteristics during the second time interval, which follows immediately. The computation is sequential, thus requiring minimum memory storage in a computer, and may conveniently be carried out on relatively unsophisticated equipment such as minicomputers.

The contained air temperature in the tire is often measured and used as an indication of overall tire heating. Its calculation requires a separate analysis given in Appendix I. From this analysis, the contained air temperature is shown to lag behind the inner surface temperature of the tire. In the initial stages of tire heating, its value is given by

$$\Delta y = \beta \Delta t (\theta - y) \quad (41)$$

where

- y = contained air temperature
- θ = weighted average of tire inner surface temperatures
- Δt = time increment
- β = a constant involving properties of the air and heat transfer coefficients.

The heat transfer coefficients chosen for the inner surface are presently based on the concepts that inner peristaltic pumping velocities are small, just sufficient to insure good mixing. This is an area where more measurements are needed.

EXPERIMENTAL PROGRAM

The problem in hand is an extremely complex one and could not be expected to be verified without considerable experimental data. A number of assumptions are used in the computation of the rate of internal heat generation in the tire, and many of these assumptions can only be verified by direct measurement of temperature fields in actual tires. For that reason a comprehensive experimental program was carried out by the Impact Dynamics Branch, Langley Research Center, National Aeronautics and Space Administration, Hampton, Virginia. Most of the work was done at the Wallops Flight Center, using a specially designed truck with a yoke and loading apparatus designed for the testing of tires.

Thermocouples were installed at the University of Michigan in approximately twenty 22 x 5.5 8-ply and 12-ply rated aircraft tires furnished by NASA Langley. Most of these thermocouple installations were done by implanting appropriate thermocouples in holes drilled in the tire carcasses after having been buffed but prior to retreading. Subsequently the tires were retreaded by a commercial retreader, and were wired for internal temperature measurements during both straight line rolling as well as cornering and braking operations. For purposes of this report only the straight line rolling data will be used. Due to load limitations of the test equipment the full rated loads of the tires could not be applied, and since it was desired to achieve normal tire deflections, inflation pressures were also kept below normal values.

Thermocouple locations are illustrated in figures 15 and 16 for the 22 x 5.5 tires.

The tire temperature data obtained from typical test runs is presented in the next section of this report where it is compared with computation. In general the use of appropriate thermocouples carefully implanted in the tire was sufficient to give a good picture of the internal temperature distribution. A thorough summary of this information is to be presented in a separate NASA document.

Due to limited load and pressure combinations which could

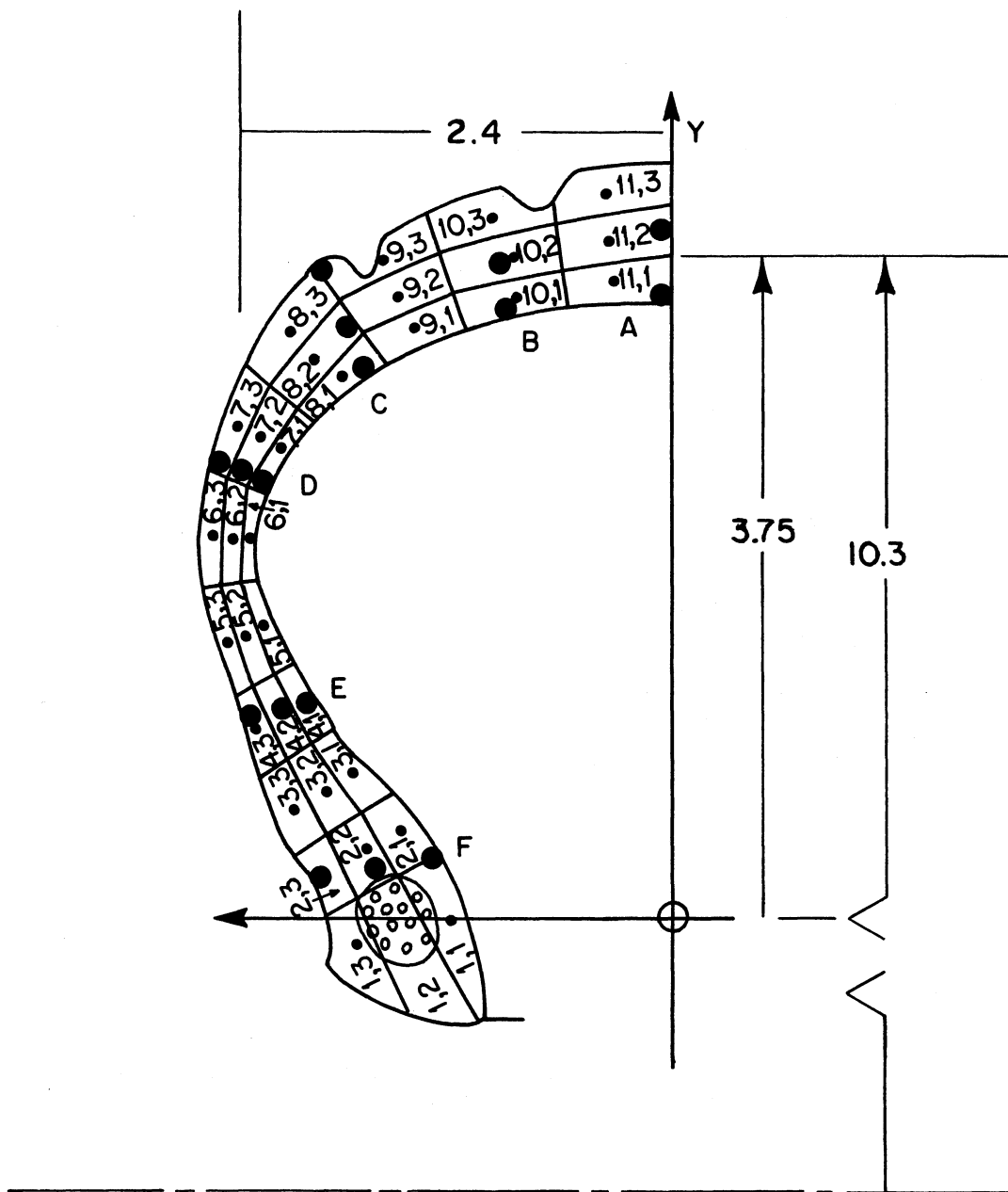


Fig. 15. Element sectioning for thermal analysis. Large solid circular symbols represent approximate thermocouple locations in the size 22x5.5, 8 PR test tires

- 6

be used on the NASA equipment, the University of Michigan conducted a series of taxi-takeoff roll tests on instrumented tires of the same size at Wright-Patterson Air Force Base, Dayton, Ohio, using their 120-inch aircraft tire dynamometer. With this equipment, full rated loads and speeds could be obtained. These data are also presented in the subsequent section and compared with computed values. These data represent a different set of temperature rise values since they involve loads, pressures, and speeds which are consistent with real operating conditions.

Referring to earlier sections of the report, it is clear that the rate of heat generation depends on the strain energy stored in the tire, which in turn depends both on bending and membrane effects. While deflection itself controls the bending contribution to this problem, the membrane contribution is clearly dependent on the inflation and thus both effects are needed to give a realistic description of tire temperature rise during service conditions.

The 22 x 5.5 tire is a relatively small aircraft tire, and since one of the most important applications of this type of calculation is to larger tires, it was felt that experimental data should also be obtained on them. Three 40 x 14 aircraft tires were also made available by NASA, and these were again fully instrumented with thermocouples at the University of Michigan. Approximately forty thermocouples were installed in each tire, using locations near the outer surface, near the carcass midline, and near the inner surface. The points of installation ranged from the crown centerline to very close to the bead. Arrangements were made to have these tires run on the large dynamometer facilities at Wright Patterson Air Force Base under the Air Force Flight Dynamics Laboratory. Full rated loads and tire deflections could be obtained there, but the tests were limited in speed in order to obtain longer thermocouple lead wire life. A complete series of tests were run on these three tires, involving various deflections at constant pressure and varying pressure at constant deflection. Thermocouple locations for these tires are illustrated in figures 17 and 18.

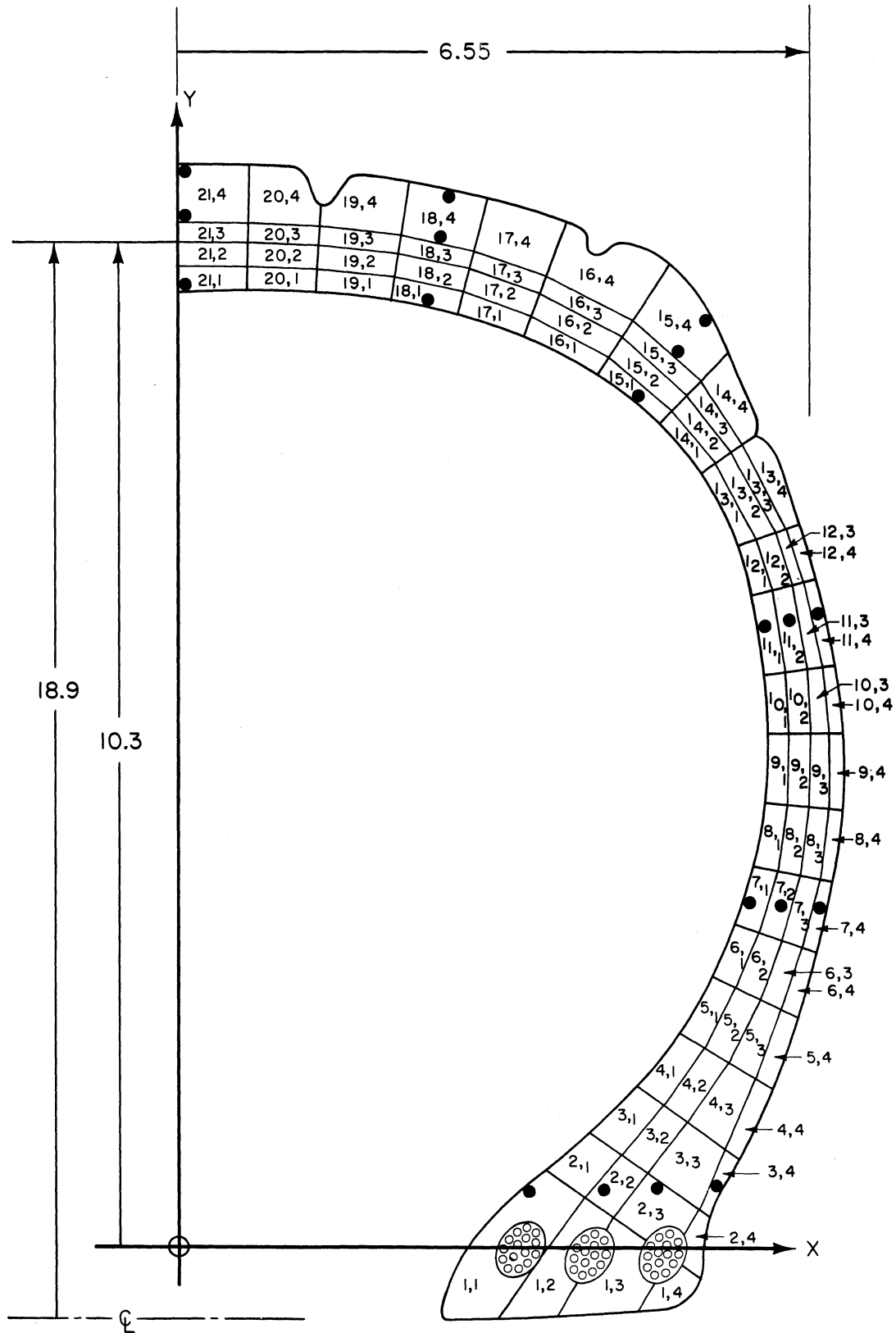


Fig. 17. Element sectioning for thermal analysis. Solid circular symbols represent approximate thermocouple locations in the size 40x14, 22 PR test tires

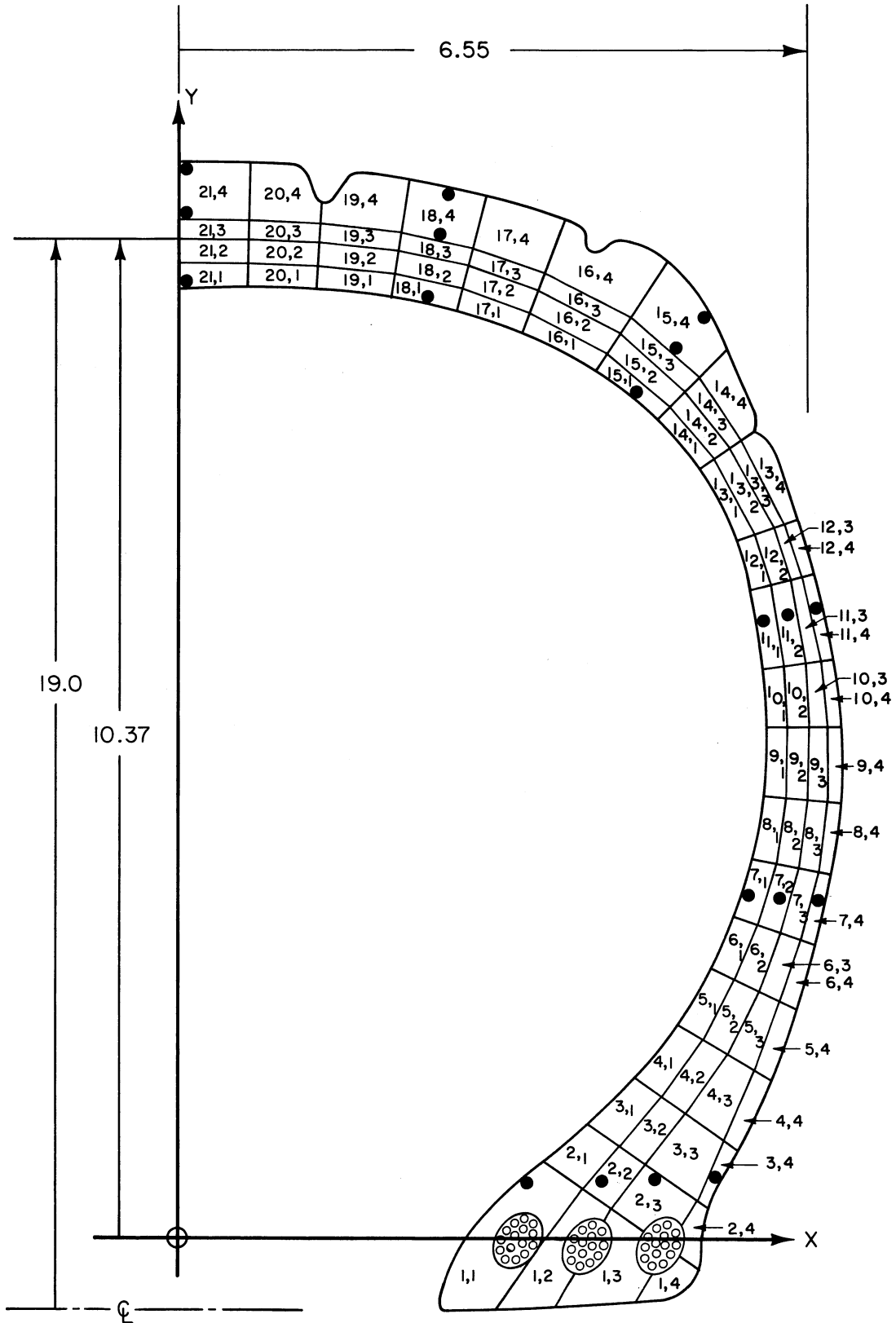


Fig. 18. Element sectioning for thermal analysis. Solid circular symbols represent approximate thermocouple locations in the size 40x14, 28 PR test tires

Tires of two ply ratings, 22 and 28, were used in this second series of experiments. Due to considerable differences in thickness of the carcass of these two tires, they are treated in this report as two separate tires.

While a great deal of temperature data were obtained by these two series of test programs, it is so voluminous that only selected parts have been used for purposes of comparison with calculations in this report. In order to provide a complete record of the test data available, however, Table 1 shows the load and speed combinations available in straight line rolling from the 22 x 5.5 NASA tests, while Table 2 shows the load, pressure and speed combinations available from the University of Michigan tests carried out on that tire size at Wright-Patterson Air Force Base.

Table 3 gives a similar summary of test conditions for the 40 x 14 tires.

Some of these data will now be extracted in detail and used in a subsequent section of this report for comparison with calculation.

Table 1
Operating Conditions NASA Langley Tests
 22 x 5.5 Tires

	Load lb	Pressure psi	Speed MPH
<u>NASA</u> <u>8PR</u>	2700	83	20
	3270	83	20
	4000	83	20
	4000	115	20
	4000	150	20
<u>NASA</u> <u>12PR</u>	2560	55	20
	3150	55	20
	4000	55	20
	4000	110	20
	4000	78	20
	4000	78	35
	4000	78	50

Table 2
Operating Conditions - University of Michigan Tests
 22 x 5.5 Tires

	Load lb.	Pressure psi	Speed MPH
<u>UM</u> <u>8PR</u>	4350	125	20
	3263	87	20
	4350	156	20
	4350	94	20
<u>UM</u> <u>12PR</u>	7100	209	20
	5325	132	20
	7100	261	20

Table 3
Operating Conditions - University of Michigan Tests
40 x 14 Tires

	Load Lb.	Pressure psi	Speed MPH
UM 22 PR	25000	175	20
	23500	160	20
	21000	145	20
	25000	175	5
	22900	155	5
	29300	160	20
	25000	175	40
	35400	160	20
UM 28 PR	33500	227	20
	30800	207	20
	27800	187	20
	33500	227	5
	30000	200	5
	38200	207	20
	33500	227	40
	46300	207	20

CALCULATION VS EXPERIMENT

Calculated temperature distributions in the tire were first compared with data measured from both the NASA tests and the University of Michigan tests. In order to carry out the computations, several material characteristics had to be estimated from the literature. These characteristics are given in Table 4.

Using a time increment of ten seconds, the computation was carried out for the temperature rise in these tires under conditions experienced by both the NASA tests and the tests conducted by the University of Michigan. Comparison between calculation and experiment is shown in Figures 19 through 24 for the thermocouple locations A through F, where the experimental data are plotted as a function of time. The computations are carried out using equation 39 and the material constants given in Table 4, along with the specific geometry for these tires.

It should be emphasized that while the outside dimensions of these two ply-rating tires are the same, their internal characteristics are quite different and hence the modeling is completely different. The elements representing the heat transfer cells are not the same, nor is the nature and extent of the carcass area. The 8PR version of the tire has only one bead, while the 12PR version has two beads. For these reasons the two sets of comparisons should be considered as being taken on two separate tires.

Similar comparisons between calculation and theory are given for the two 40 x 14 tires, and again plots of temperature rise are used as a basis. These data are presented in figures 25 through 36. The material constants used for the 40 x 14 tire are also given in Table 4 and once more some of the input data must be estimated from literature sources.

Table 4

Material Characteristics of
22 x 5.5 and 40 x 14 Aircraft Tires

Region*	E psi	G psi	$\tan\delta_o(3)$	α Degrees	K	ρ	C_p
ead (II)	(1)	335	0.15	-	5×10^{-4}	1.0	0.5
rcass , III)			0.15	(2)	5×10^{-4}	1.0	0.5
dewall bber (IV)		335	0.15			1.0	0.5
ad (V)	15×10^6		0.03				

* See fig. 6

(1) See Appendix E. For shear modulus G of rubber use 335 psi.

(2) Calculated by cosine law using $\alpha = 35^\circ$ crown angle.

(3) Values of $\tan\delta_o$ are given for 25°C . For higher temperatures, $\tan\delta$ is calculated by the approximate expression

$$\tan\delta = \tan\delta_o e^{-.01\Delta\theta}$$

where $\Delta\theta$ is the temperature rise in $^\circ\text{C}$ above ambient.

E = Young's modulus of rubber, psi G = Shear modulus of rubber, psi α = Cord angle, deg.

K = Thermal conductivity, $\frac{\text{cal}}{\text{cm}^\circ\text{C-cm}^2\text{-sec}}$ ρ = Density C_p = Specific heat

It should be emphasized that some of the input data needed for these computations is not readily available to the casual user of this program. In particular this holds true for the quantity $\tan \delta$, which directly controls the rate of heat generation. This quantity is not well known for cord-rubber composites, and in this case it has been estimated from test data on similar composites. Both the strain and temperature dependence of $\tan \delta$ are also important. We have attempted to estimate the temperature dependence term from very sketchy published data. The strain dependence is left undefined, but known to be a large effect. These shortcomings point up the need for continued research in material properties of cord-rubber composites.

Bending stiffness of the composite sidewall of the tire is important, particularly in the area near the bead. It is very difficult to calculate this quantity with any accuracy since it depends strongly on the location of the neutral axis, which, in turn, is influenced by the state of tension in the cord-structure. Experiments show bending stiffnesses which are many times smaller than those which would be predicted by simple beam or plate calculations based on properties measured in tension. For this reason care should be taken in the bead region of the tire to insert proper bending stiffnesses.

Runway friction influences to some extent the membrane stresses in the center of the tire contact patch. This is very difficult to estimate quantitatively. It is discussed analytically in Appendix J, but the actual friction levels available in the tests which are quoted can only be estimated in calculation.

As can be seen from figures 19 through 36, the calculations generally agree well with the experimental data over a wide range of inflation pressures and tire deflections. In particular the calculations predict the ranking of hottest areas in the tire at a particular location, i.e., from outside to inside and vice-versa. Further, the calculations support the reversal of inside-outside temperature gradient between sidewall and tread, a phenomenon observed experimentally.

From a study of the comparisons between these computations and the experimental data, it is concluded that the major trends in the temperature rise problem can be calculated adequately for relatively short term taxi-takeoff conditions. More emphasis must be placed on obtaining good thermal properties of the materials and better heat transfer coefficients in order to improve the accuracy of the predictions.

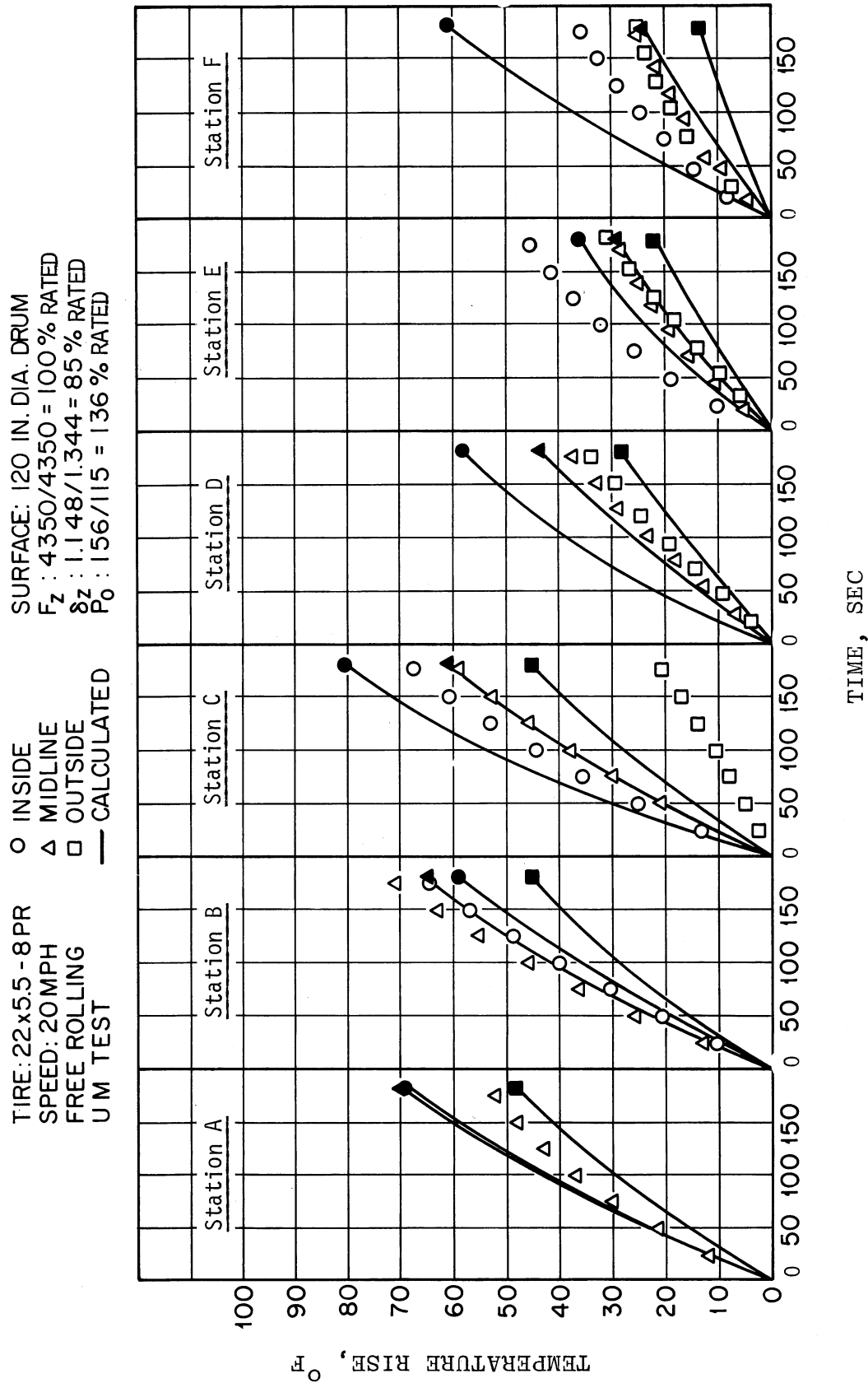


Fig. 19. Measured and calculated tire temperature profiles

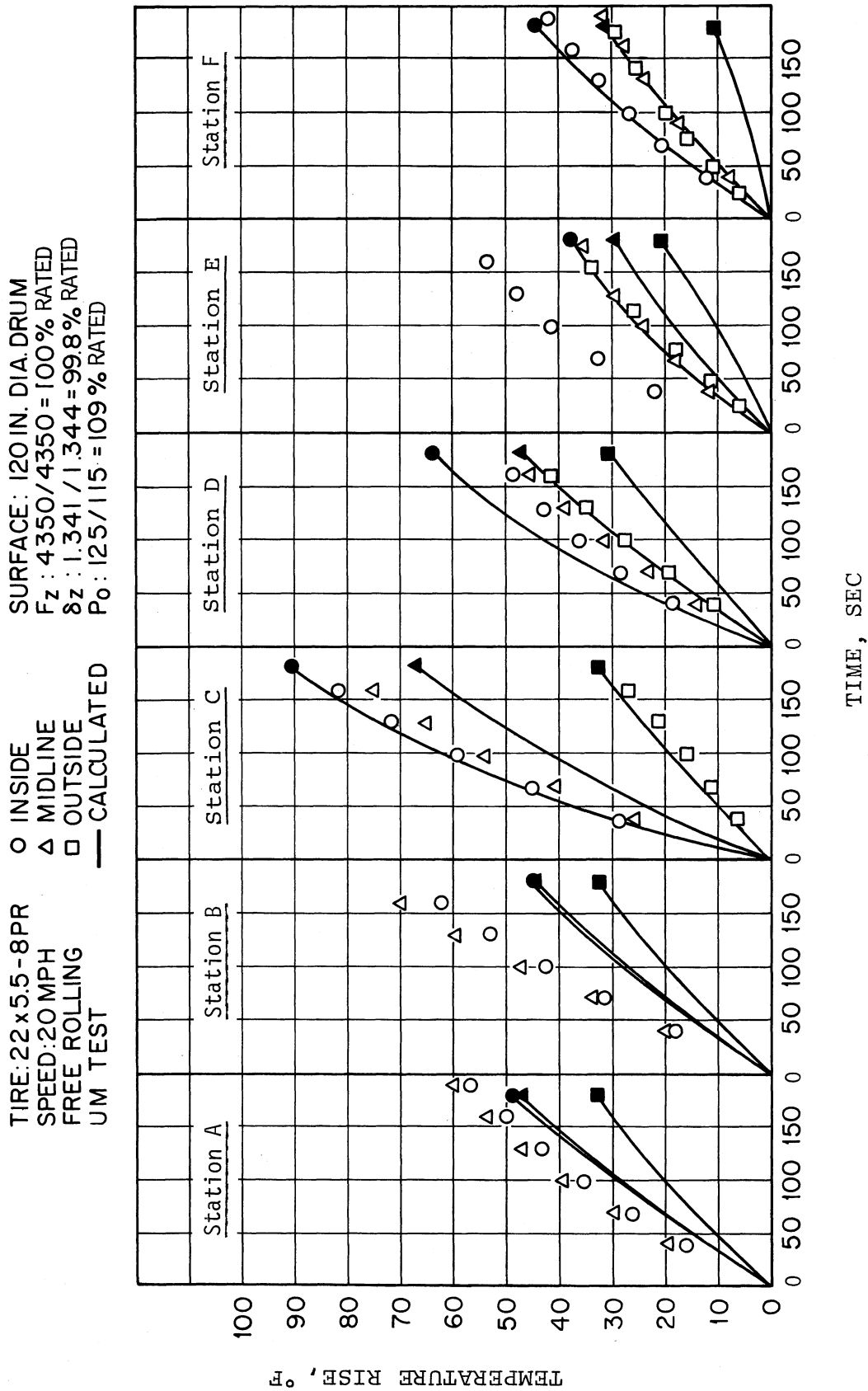


Fig. 20. Measured and calculated tire temperature profiles

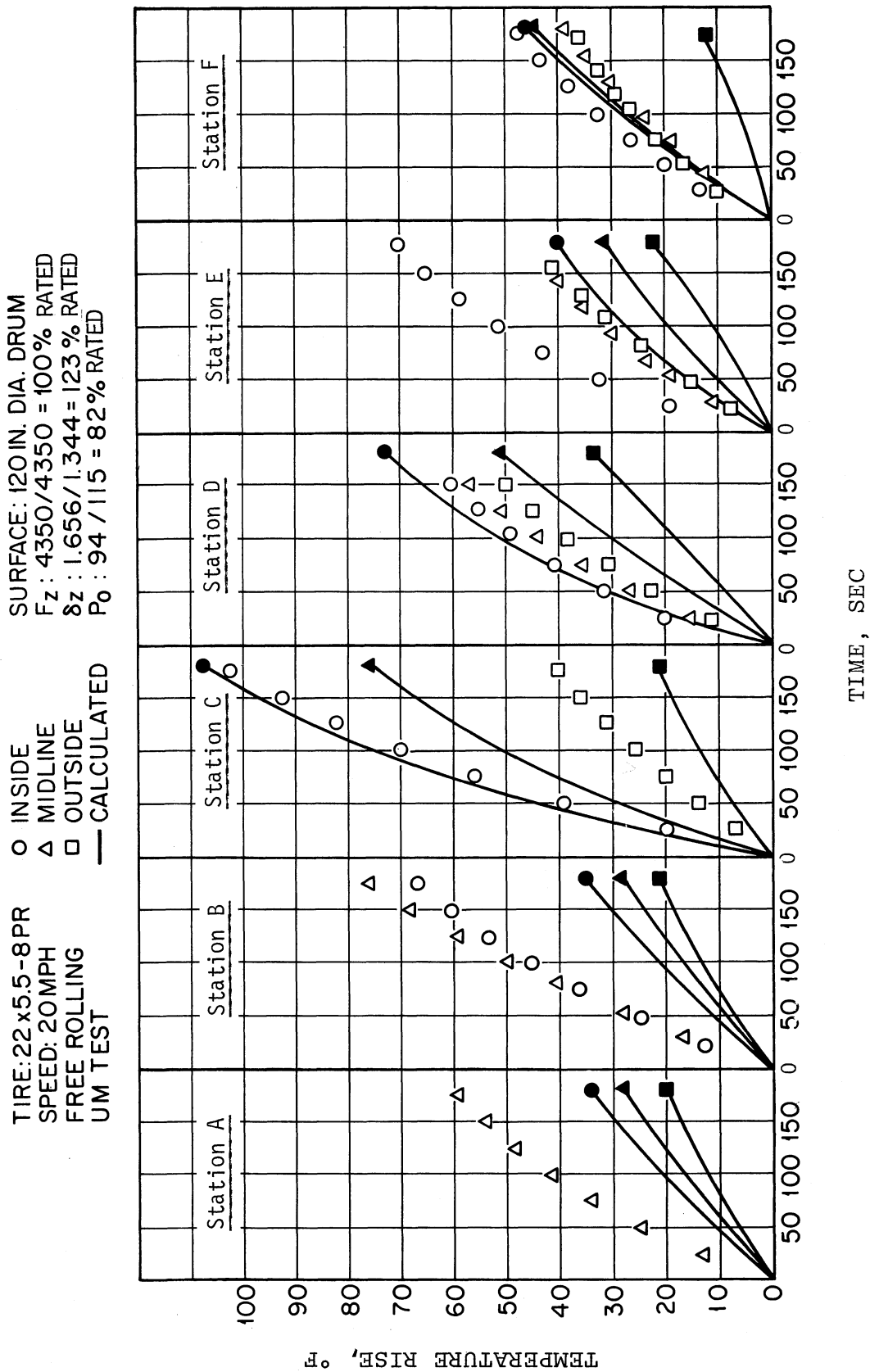


Fig. 21. Measured and calculated tire temperature profiles

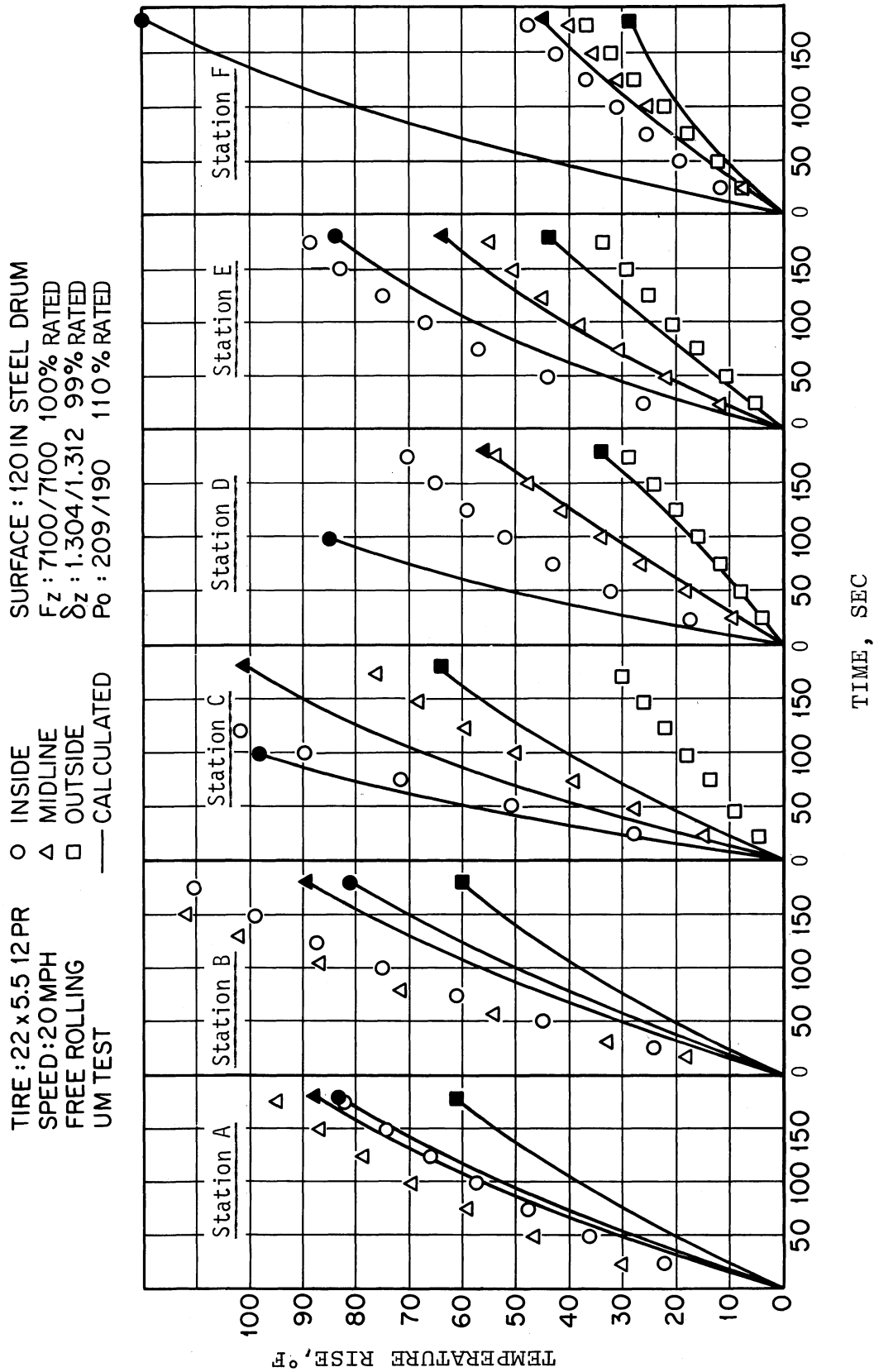


Fig. 22. Measured and calculated tire temperature profiles

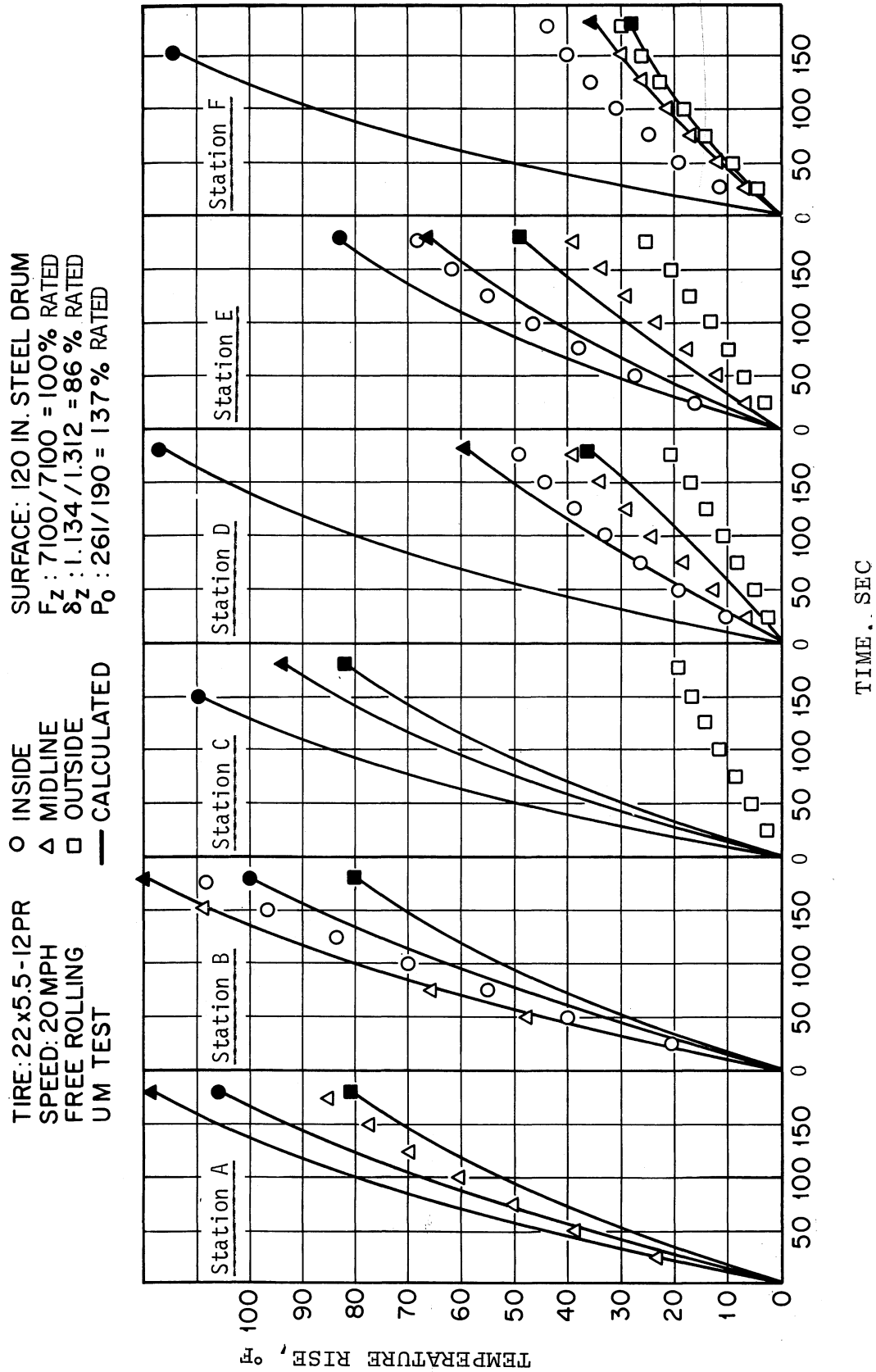


Fig. 23. Measured and calculated tire temperature profiles

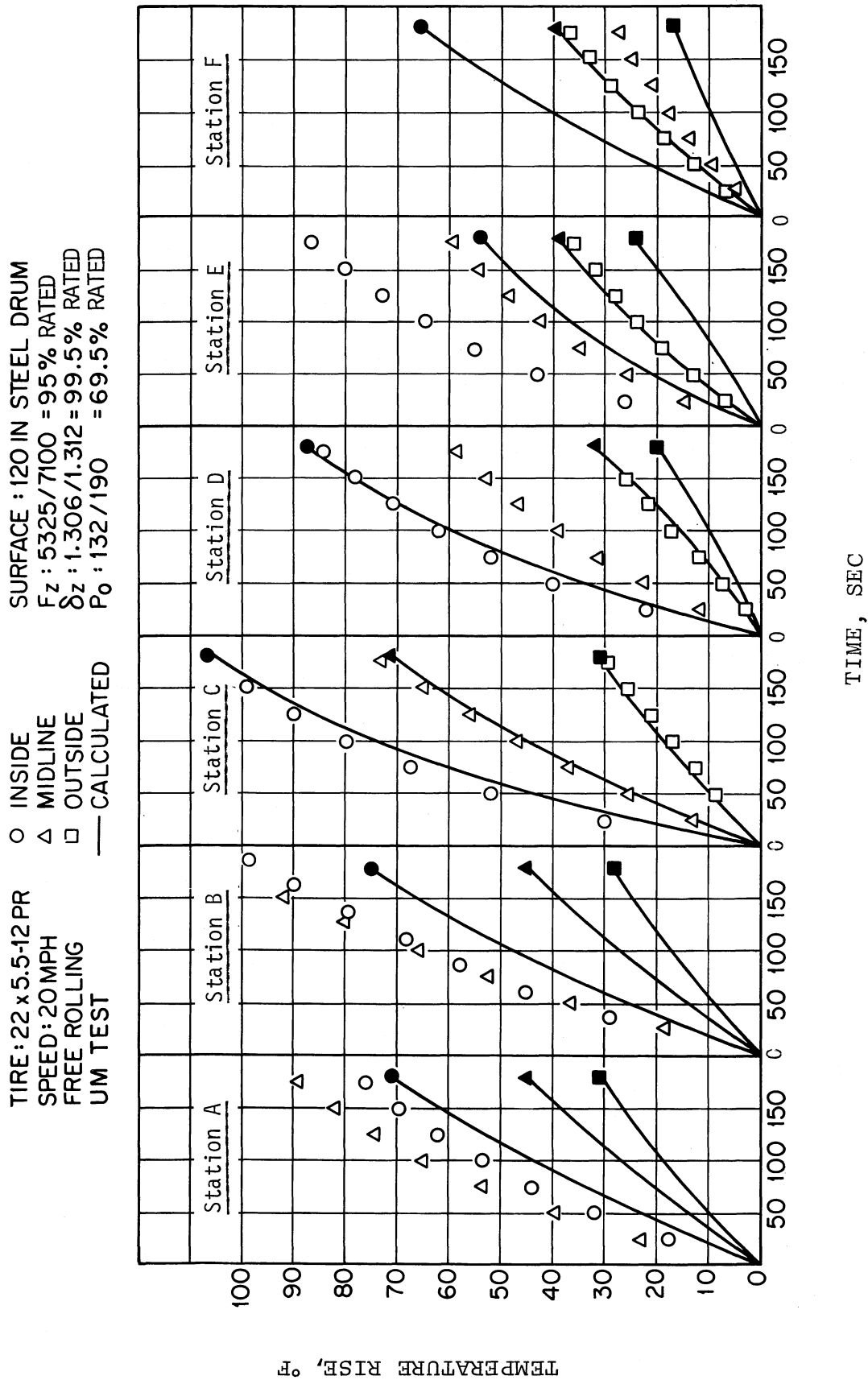


Fig. 24. Measured and calculated tire temperature profiles

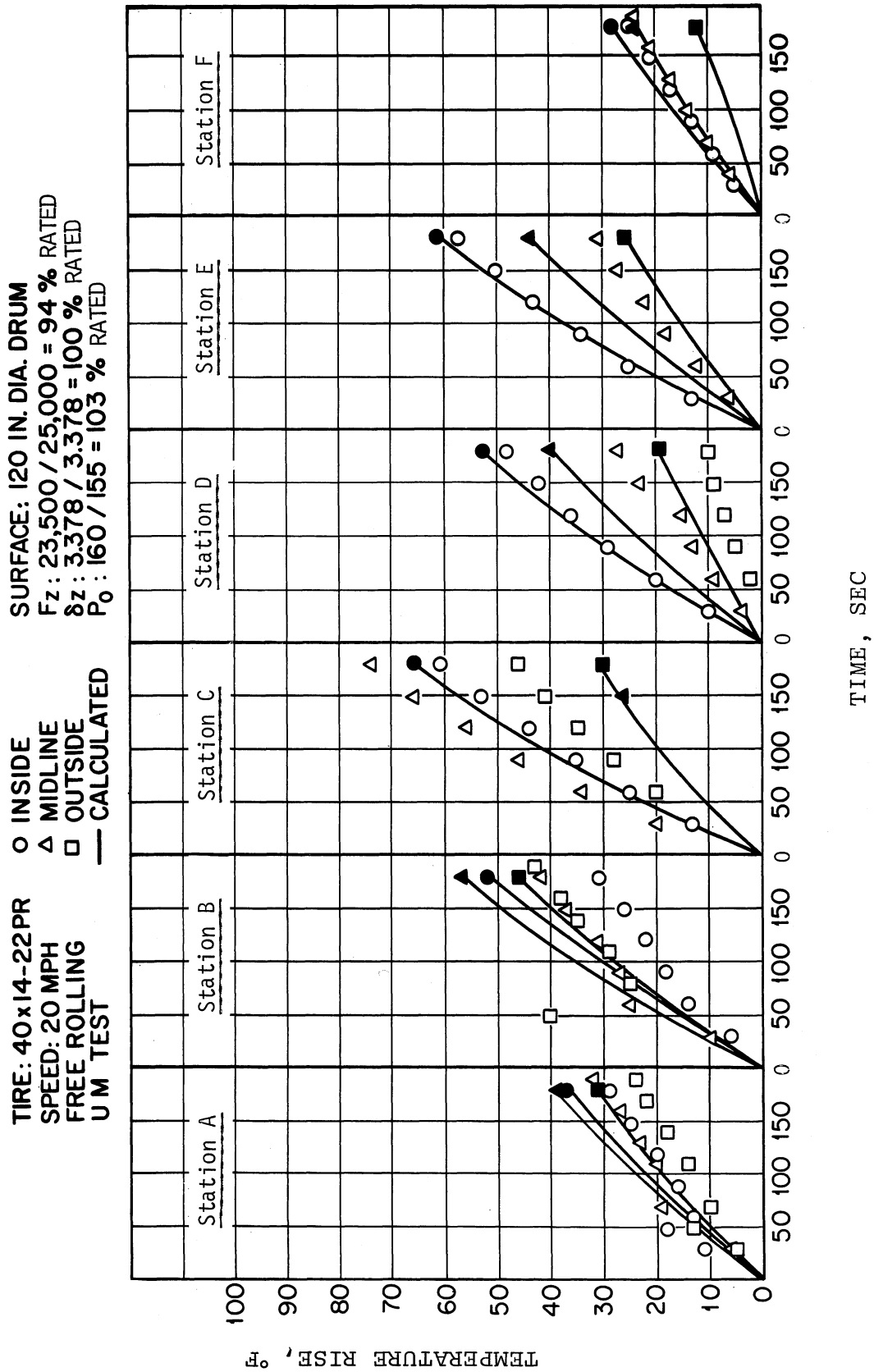


Fig. 25. Measured and calculated tire temperature profiles

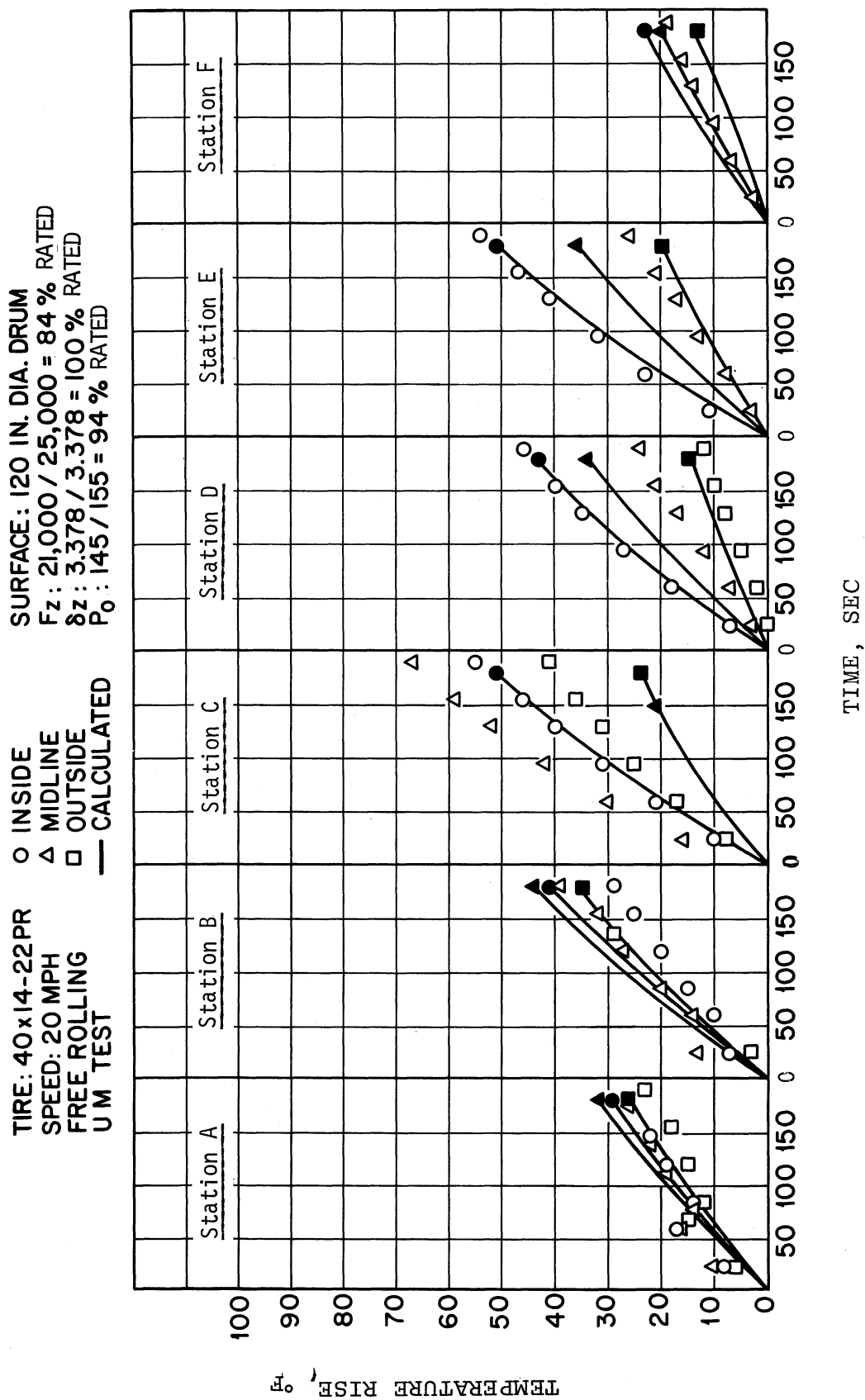


Fig. 26. Measured and calculated tire temperature profiles

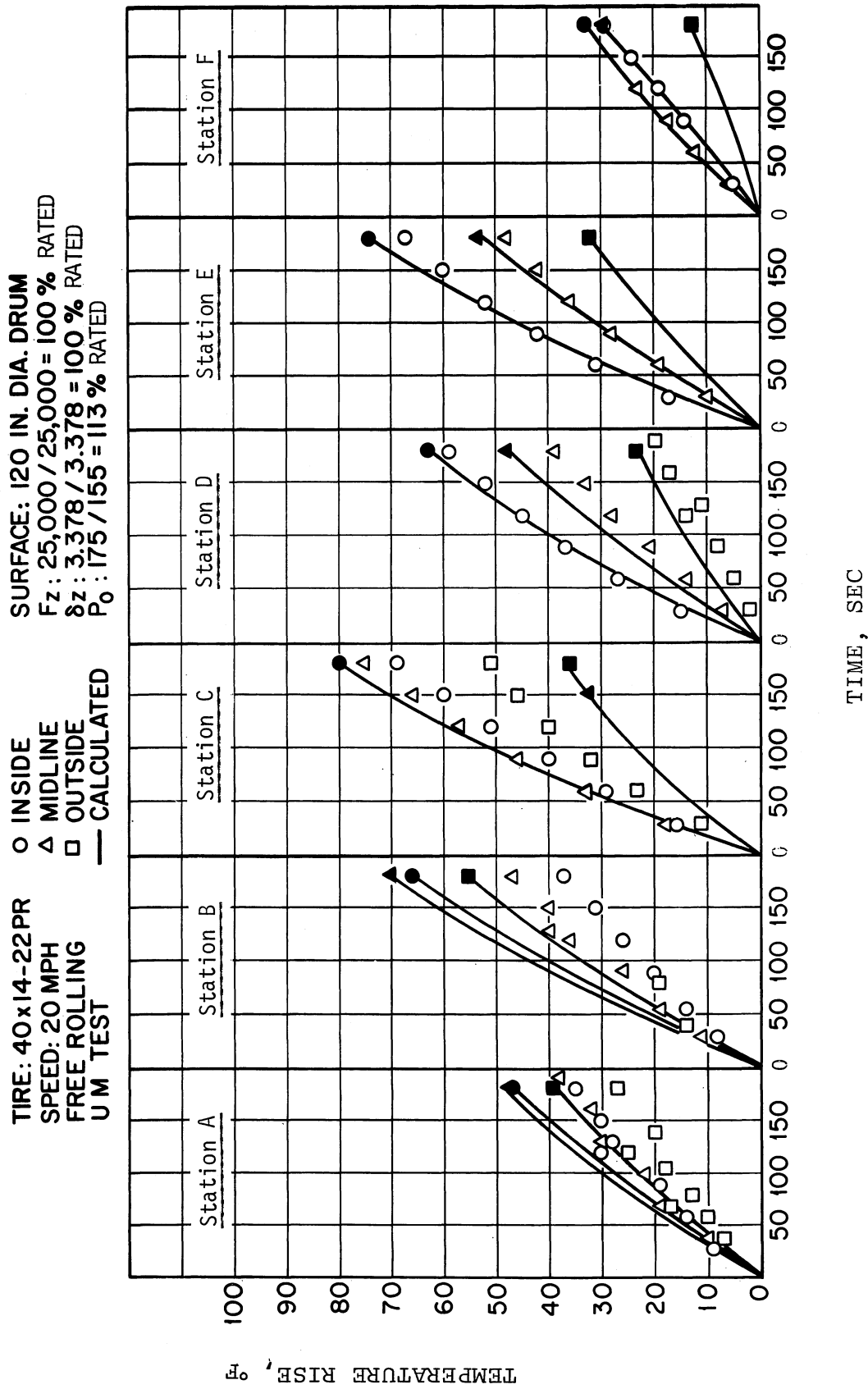


Fig. 27. Measured and calculated tire temperature profiles

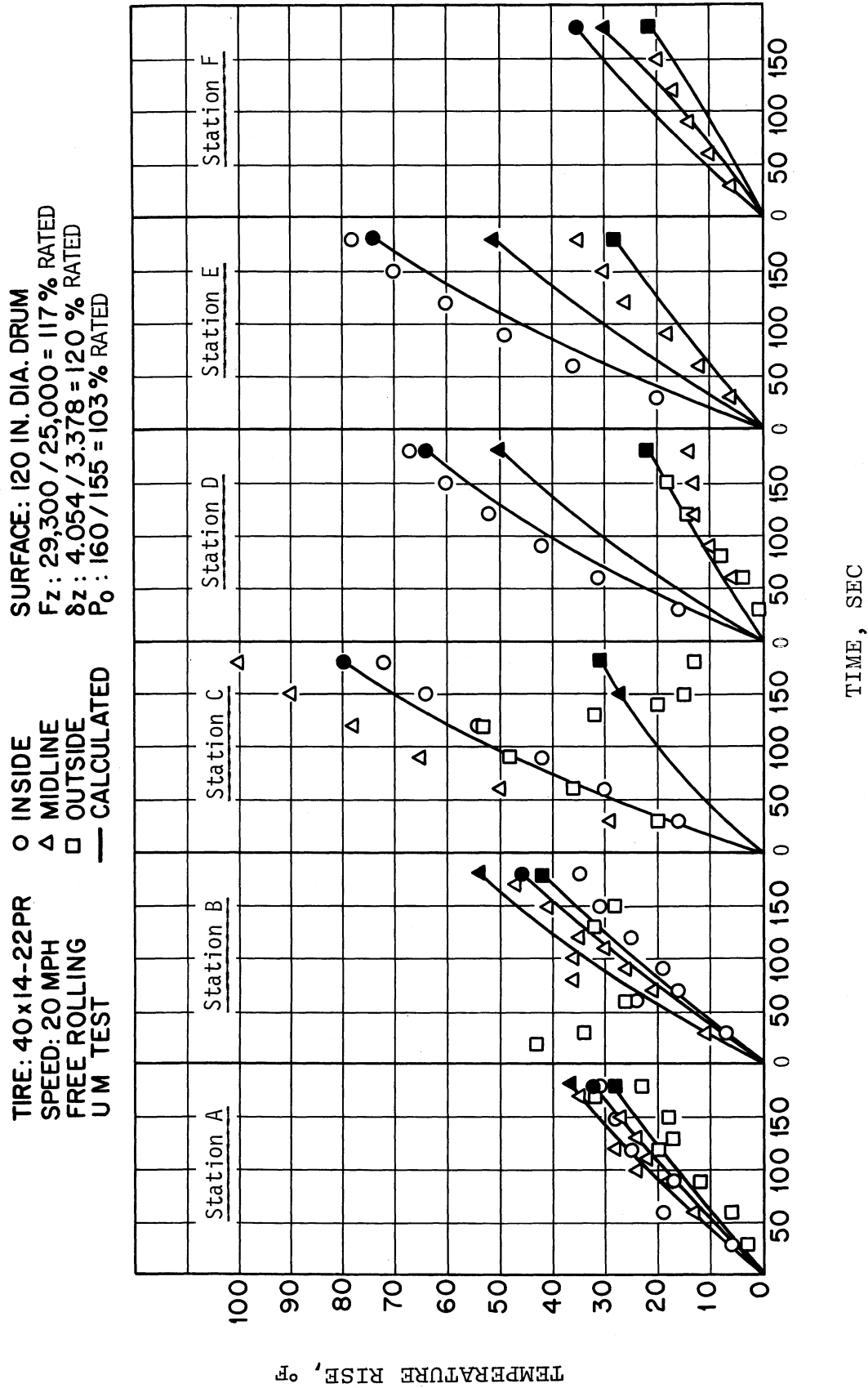


Fig. 28. Measured and calculated tire temperature profiles

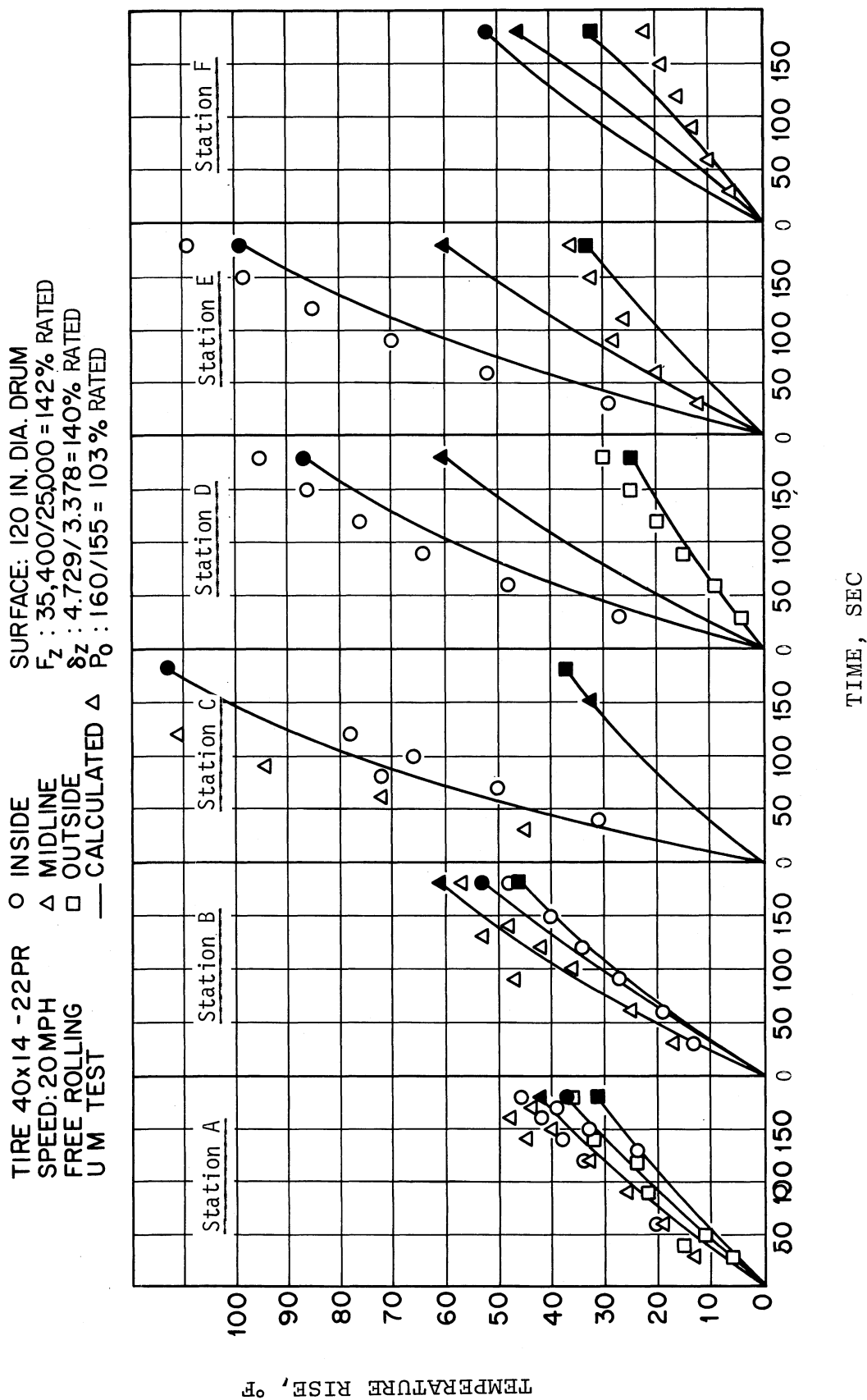


Fig. 29. Measured and calculated tire temperature profiles

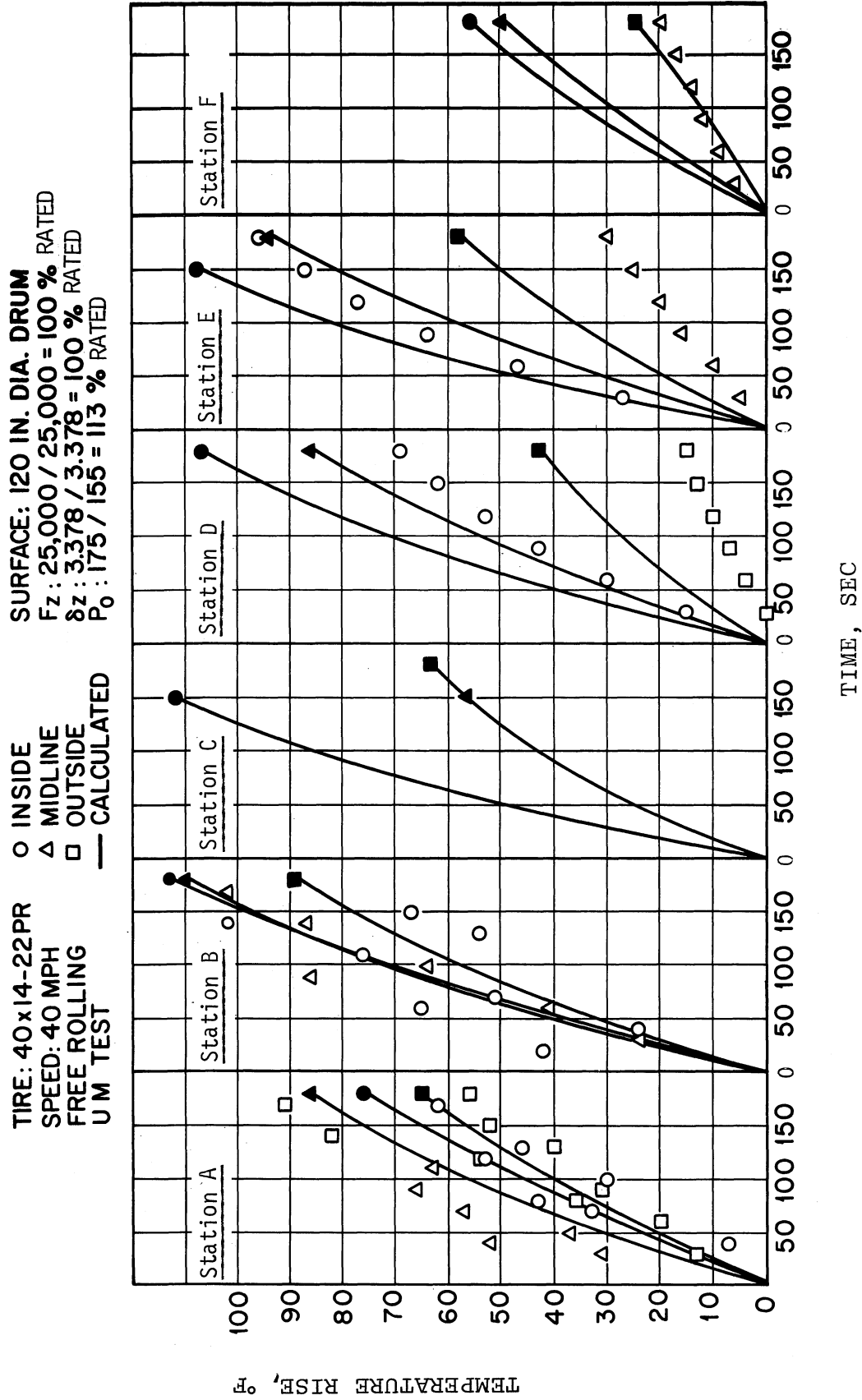


Fig. 30. Measured and calculated tire temperature profiles

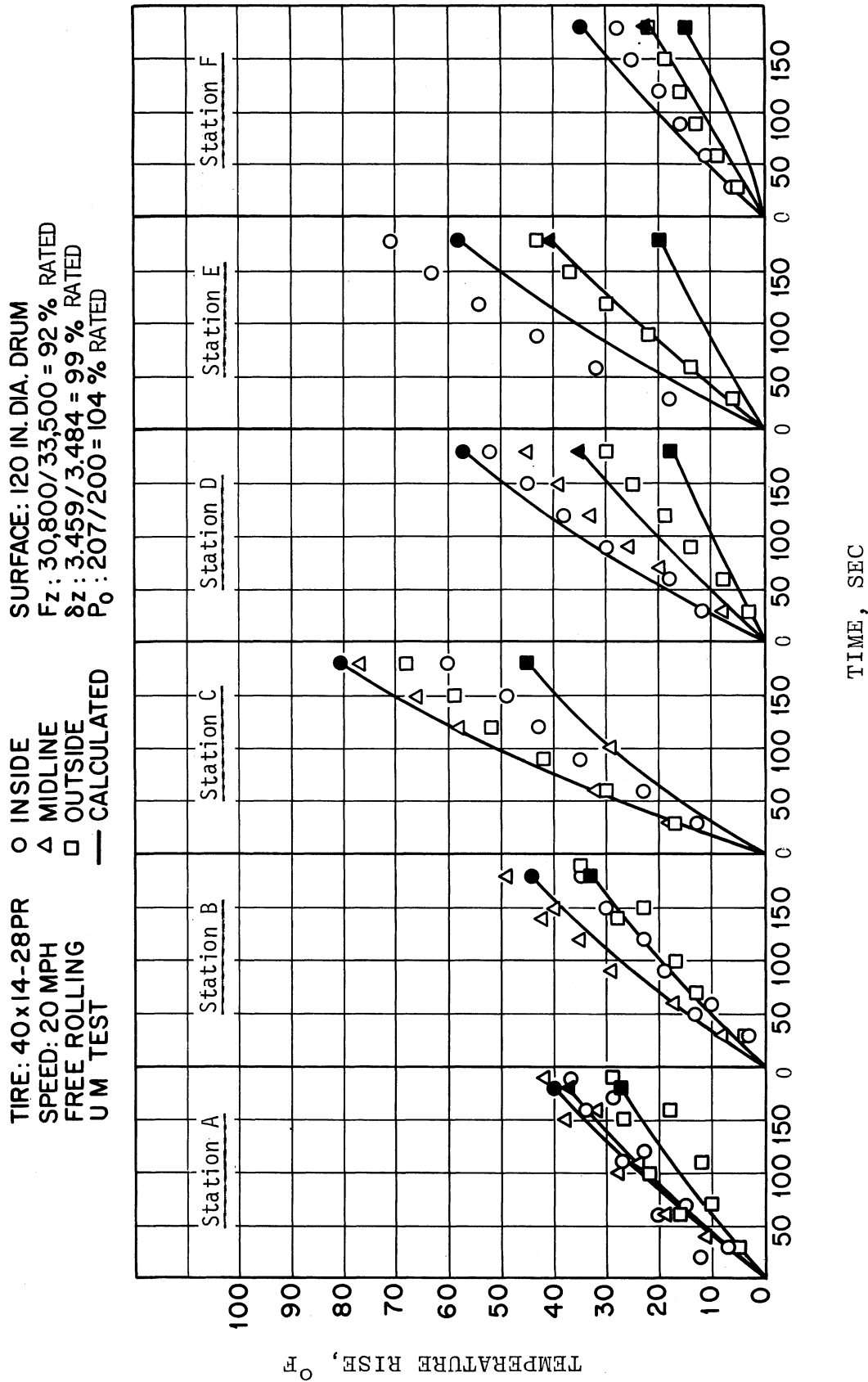


Fig. 31. Measured and calculated tire temperature profiles

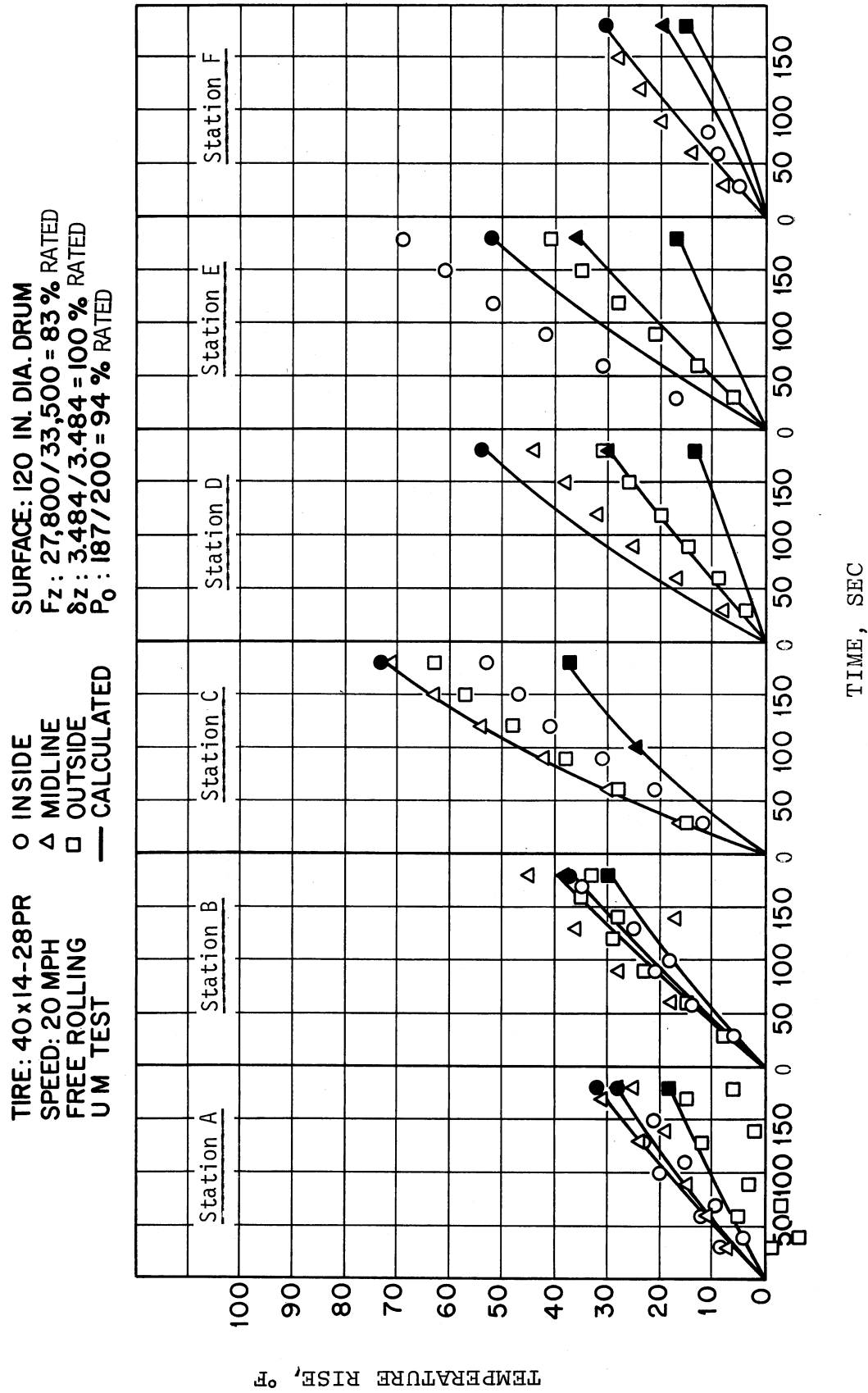


Fig. 32. Measured and calculated tire temperature profiles

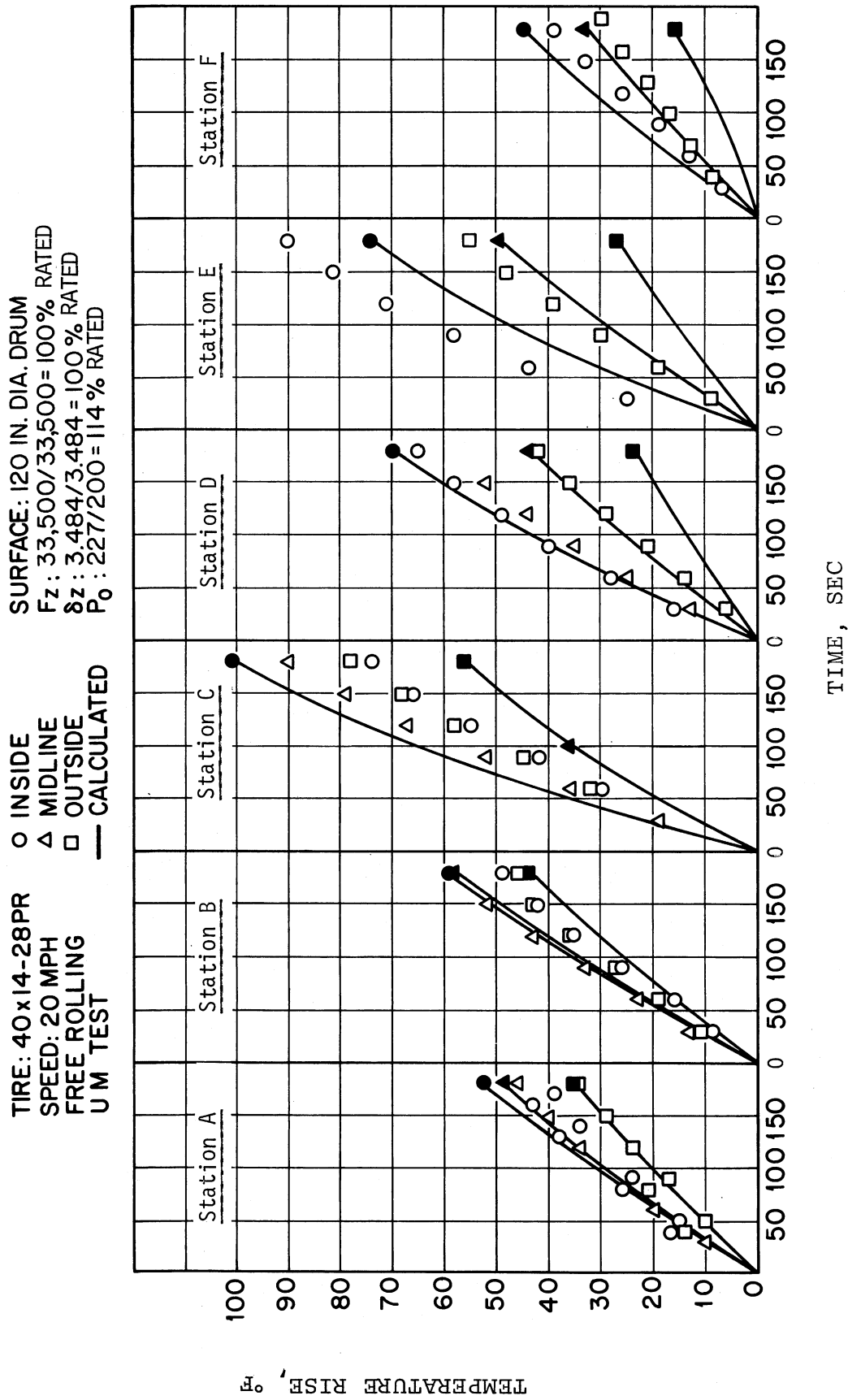


Fig. 33. Measured and calculated tire temperature profiles

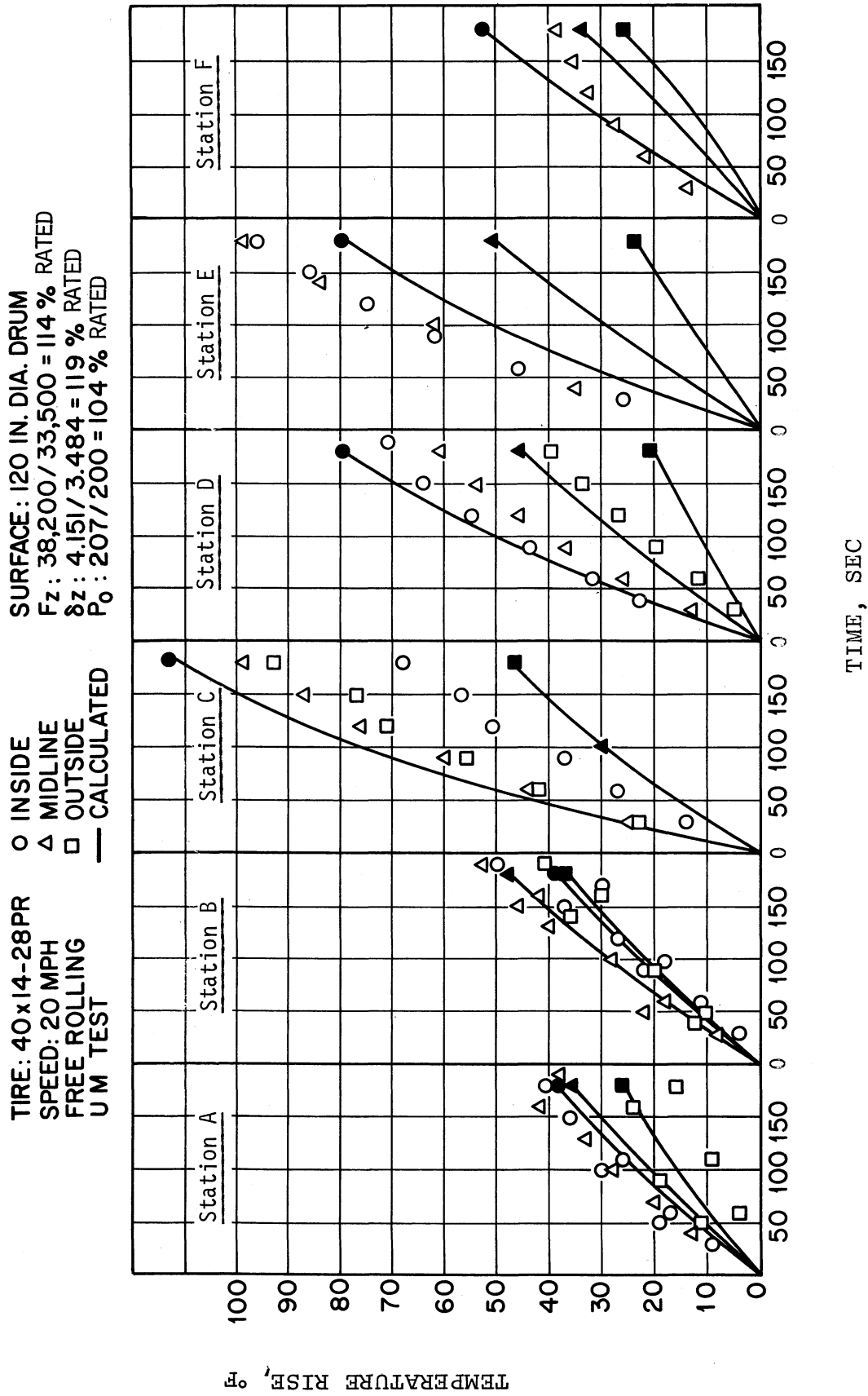


Fig. 34. Measured and calculated tire temperature profiles

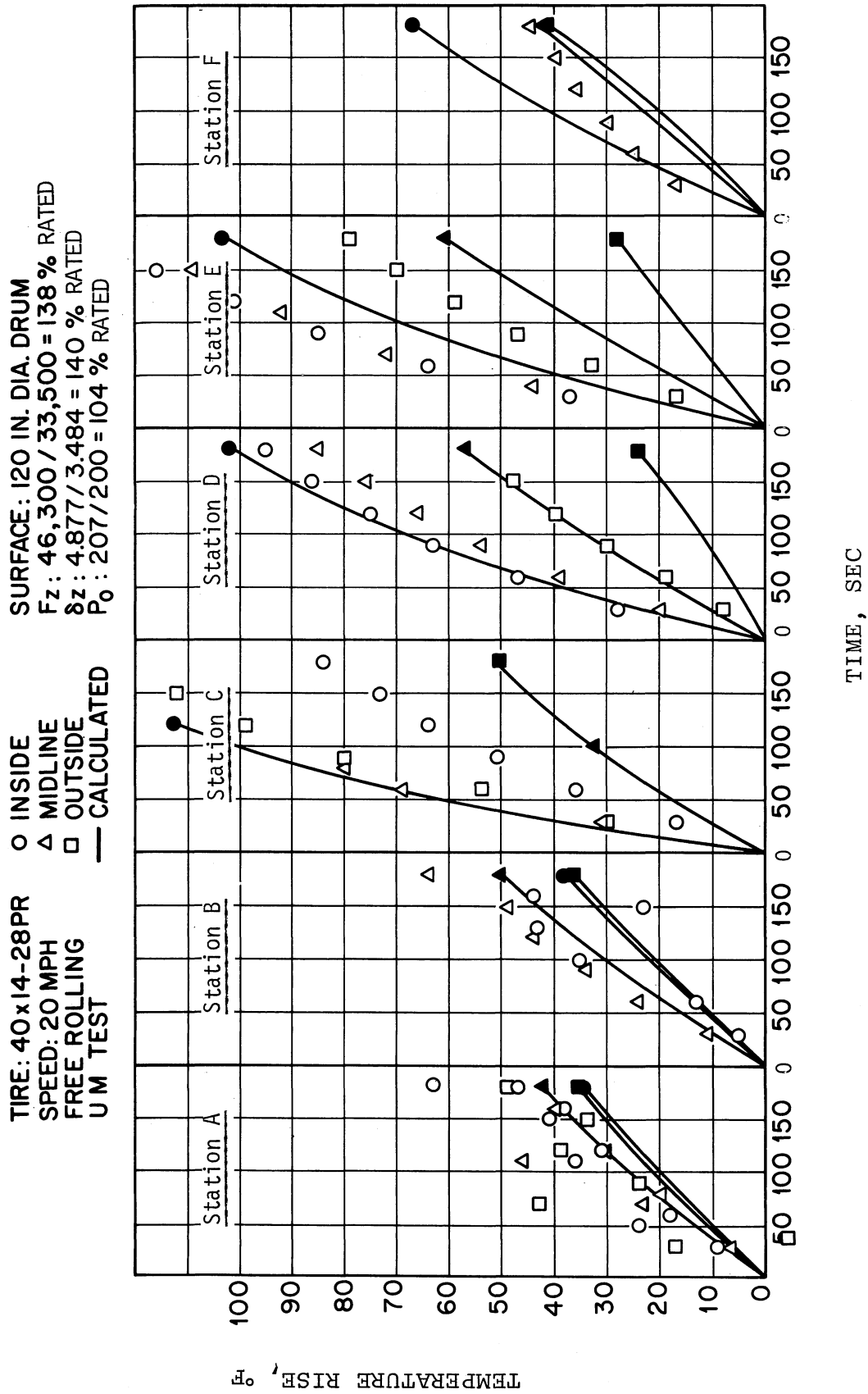


Fig. 35. Measured and calculated tire temperature profiles

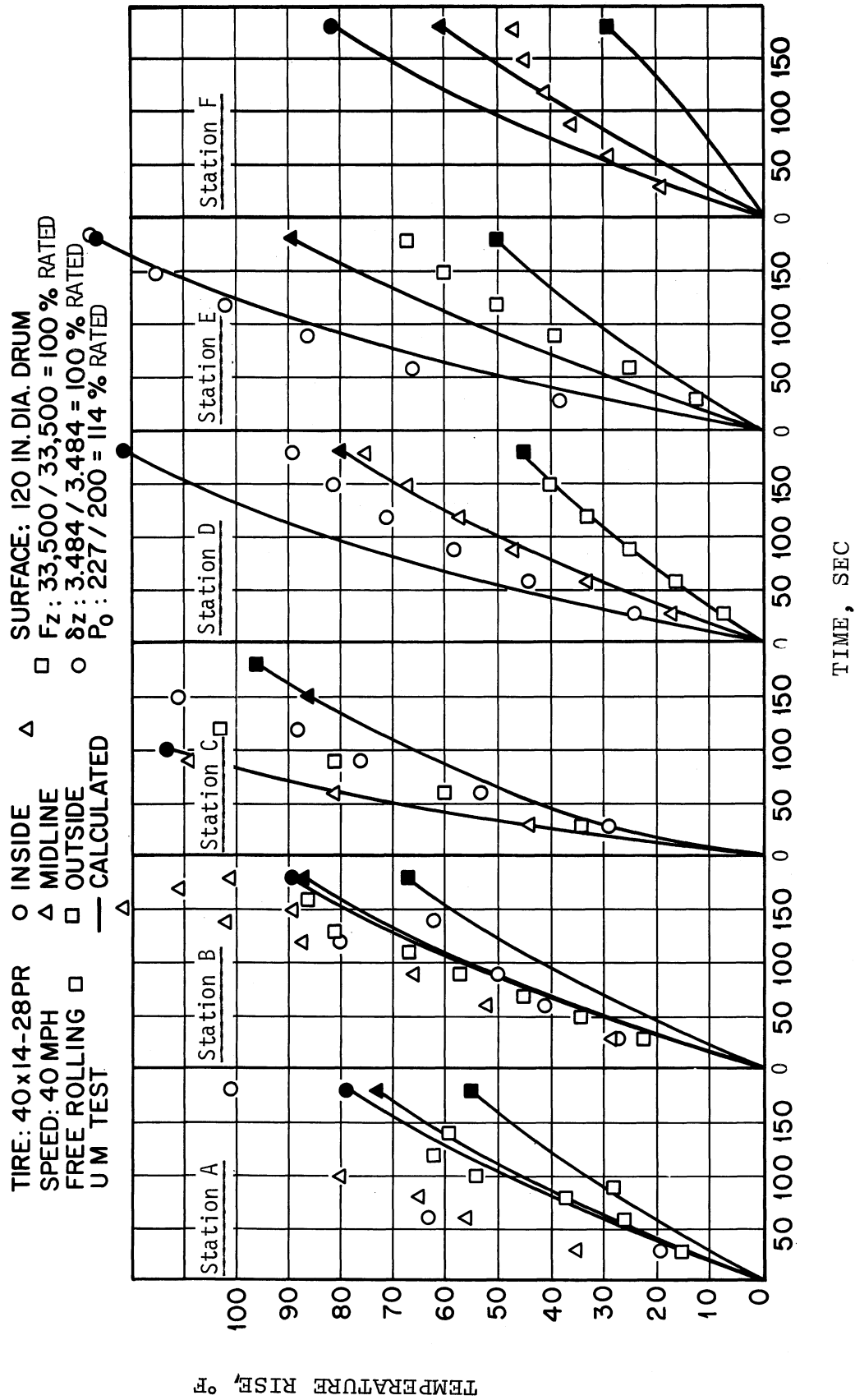


Fig. 36. Measured and calculated tire temperature profiles

CONCLUSIONS

A method has been developed for approximating the internal temperature distribution in an aircraft tire due to unyawed free rolling under load. The method is based on an approximate stress analysis of a material point in the tire as it rolls through the contact patch. From this analysis the mechanical work done on the material point is converted into the heat generated due to the loss characteristics of the materials at that point. Thus, each material point of the tire has its own cyclic heat generation each time it rolls through the contact patch and is stressed. Furthermore, due to the high frequency of cyclic stressing compared with the relatively slow diffusion times of heat in polymeric materials, the temperature distribution in the tire is considered to be axisymmetric.

With a rate of heat generation established at each material point on the cross section of the tire, heat diffusion throughout the carcass is calculated by the usual numerical methods which will involve loss of heat in the tire through various mechanisms such as convection at the outer and inner surfaces, conduction through the bead area into the flange of the wheel, and conduction through the tread surface into the runway material. All of these mechanisms modify the normal diffusion process so that at any time tire internal temperatures are dependent not only upon internal rates of heat generation but also on the appropriate loss characteristics at the tire surfaces.

An extensive experimental program was carried out jointly between the University of Michigan and the Impact Dynamics Branch, Langley Research Center, NASA. This program consisted of temperature measurements made at internal points in 22 x 5.5 and 40 x 14 size tires, each with two different ply ratings. Due to differences in dimensions, section thickness and in distribution of cords, these four tires each require a completely separate geometric and material property description. Some of the experimental data were taken at the NASA Wallops Flight Center using the NASA tire test truck, operating on asphaltic and concrete runway surfaces. The University of Michigan data were taken on the 120-inch steel dynamometer drum at Wright Patterson AFB, Ohio, where higher tire loads could be obtained. The data presented in this report are mostly taken from these latter tests.

All data were obtained from thermocouples buried in the tire carcass prior to retreading the tires. These thermocouples were connected to conventional recording apparatus, and gave continuous readings of tire temperature at selected internal points.

Experimental data from these measurements are compared with data calculated over a wide range of tire loads, inflation pressures, speeds, and deflections. Generally speaking, the analytical model gives good agreement with measured values when the tire is operating in the range of its normal rated load, pressure, and deflection.

REFERENCES

- . Carslaw, H. S.; and Jaeger, J. C.: "Conduction of Heat in Solids". Second ed., Oxford University Press, Inc., 1959.
- . Clark, S. K.: "Plane Elastic Characteristics of Cord Rubber Composites". Textile Res. Jour., vol. 33, 1963, p. 295.
- . Walter, J. W.: "Cord Rubber Tire Composites". Rubber Chem. and Tech., vol. 51, no. 3, July-Aug. 1978, p. 524.
- . Hoffenberth, W.: "Zür Festigkeit Des Luftreifens". Kautschuk Umb. Gummi, vol. 9, 1956, pp. 225-231.
- . Smiley, R. F.; and Horne, W. B.: "Mechanical Properties of Pneumatic Tires With Special Reference to Modern Aircraft Tires". NASA TR R-64, 1960. (Supersedes NACA TN 4110.)

APPENDIX A

Energy Loss as Related to Strain Energy

The question of the formulation of the hysteretic loss in materials is not well defined in the literature. Elementary considerations, such as discussed in the body of this report, imply that hysteretic loss may be expressed as a fraction of strain energy. In the case where the hysteretic loss is caused by cycling between two non-zero stress states, it is not immediately clear whether the appropriate strain energy is the 0-1-2-4 area or the area 1-2-3 shown in Fig. A1.

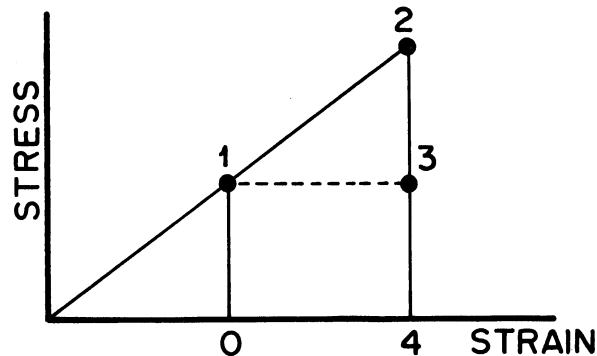


Fig. A1. Idealized stress strain curve

In order to resolve this question, loss characteristics of a typical bias cord-rubber composite were measured over a range of prestrains using a constant cyclic strain excursion. If the strain energy upon which loss is based is the area 0-1-2-4 of Fig. A1, then the hysteretic loss should increase with prestrain. On the other hand, if the area 1-2-3 defines the appropriate strain energy then the hysteretic loss should be independent of prestrain. The results of the experimental program showed a constant $\tan \delta$ over a range of prestrains, thus validating the concept that the appropriate area is 1-2-3. Details of the experiment are given in Table A1.

Table A1

Details of strain energy experiments

Test	A	B	C	D	E
Prestrain (in)	0.2	0.4	0.6	0.8	1.0
Stroke (in)	± 0.1	± 0.1	± 0.1	± 0.1	± 0.1
$\tan \delta$	0.151	0.147	0.148	0.144	0.139

specimen: 1000/2 Polyester cord in Rubber Cylinder 2.6 in.
diameter x 15 in. long. Frequency 10 Hz.
Cord angle 45° . Loading axial.

APPENDIX B

Cross-Section Curvatures

As discussed in the body of the report, the inflated shape of the tire cross-section must be obtained for the purpose of determining the geometry of the midline of the tire carcass. This geometry enters into the computation of the membrane stresses.

Several different methods were examined for determining the cross-section shape. Since aircraft tires in general are of bias construction, the Hofferberth equations of reference 4 were examined for their accuracy of prediction. It was found that they did an adequate job of predicting the inflated shape of the tire in its upper half, in the vicinity of the tread and shoulder region, but seem to fall quite short of good accuracy near the lower sidewall and bead area where rim and bead constraint effects were greater. Deviations in these regions were large enough so that the Hofferberth equations were deemed inadequate.

An examination of the differences in such tire dimensions as overall diameter and section width between the uninflated and inflated tires showed that these were sufficiently small to the extent that to a good approximation the tire cross-sectional shape when inflated, could be approximated from its uninflated cross-section. Using sections cut from the tire and making appropriate changes for the effect of inflation, the radial positions of the various element centroids could be approximated, as could the tangent angles needed for computation such as shown in Fig. 3.

Such drawings were made for both types of 22 x 5.5 and 40 x 14 tires. Examination of these drawings showed that the sidewall region can be approximated rather well by a single circular arc beginning at the bead and ending at the edge of the tread. The tire carcass centerline in the tread region can also be fit by another circular arc segment blending into that used for the sidewall. Such a representation has some advantages since it allows rapid calculation of membrane stress levels.

Calculation of the tire deformed shape requires considerably more effort. In the case of the tread region, the tire cross-section is considered to be flat and in complete contact with the runway surface. However, the sidewall region is severely deformed.

The point of demarcation between the tread and sidewall region is clearly defined in most aircraft tires by the molded pattern of the tread elements. In the cases of all four tires used for this study this point is clearly evident, allowing it to be marked.

The region outside of contact deforms substantially, and one method of obtaining an accurate picture of the geometry of this deformation is the use of two-dimensional finite element programs suitable for handling large deformation processes. Again one of the shortcomings in such a use is lack of good elastic property data on the composite carcass stiffness.

A simpler computation scheme can also be employed. The tire sidewall can be considered to be a curved arch as shown in Fig. B1, and loads can be applied to the upper end of the arch sufficient to cause the known deflections which must take place there, as determined by the deflection imposed on the tire. Fig. B1 illustrates the geometric variables involved here.

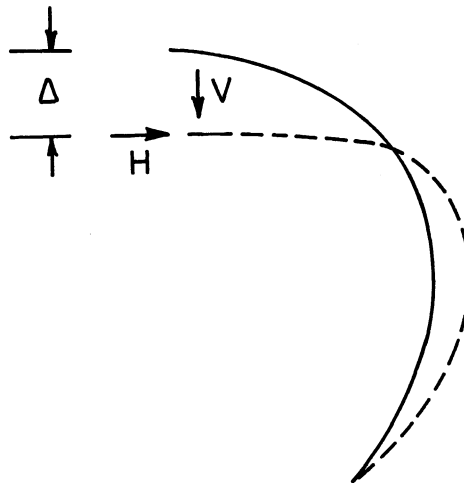


Fig. B1. Geometry of curved arch

If the bending stiffness of the arch is known at the various points throughout its length, then linear energy analysis should be sufficient to determine the values of the loads needed for this deflection. From these loads, changes in radii of curvature can be obtained, as well as deflections of the intermediate points. By a similar analysis, the tangent angle of the deformed shape can also be obtained. Such an analysis was carried out for both the 22 X 5.5 and the 40 X 14 tires, and these shapes showed relatively good agreement with the known section widths of these tires at the center line of their deflected contact patch.

In both cases it was necessary to modify the usual calculation somewhat. The linear computation of such large deflections results in an unacceptably large change in arc length of the curved beam. For that reason, the vertical deflections were calculated by the usual linear method, and the horizontal deflections were obtained by assuming that the arc lengths between each of the elemental points were held constant. A typical cross-section drawing for a 40 X 14 tire in its undeformed and deformed position is shown in Fig. B2.

Finally the simplest method for representing the sidewall shape is to consider the relatively thin sidewall as a membrane enclosing a two dimensional opening extending from the bead to the edge of the tread region in contact with the runway. This membrane will form a circular arc whose radius can be determined from the length using an average curvature, which can then be used to estimate both bending and membrane effects as tire deflection or pressure vary.

If one uses the circular arc model for both deformed and undeformed tire shapes, then much of the needed tire geometry can be calculated from the arc properties.

It is assumed that the geometry of the tire carcass can be described by two intersecting circular arcs. For the undeformed tire these arcs describe the carcass centerline from the crown of the tire to the shoulder, R_c , and from the shoulder to the bead, R_1 , as shown in Figure B3.

It is assumed that the x-y coordinates of the shoulder (x_c, y_c) and bead (x_b, y_b), the y-coordinate of the carcass at the crown, y_m , and the length of the carcass centerline from the

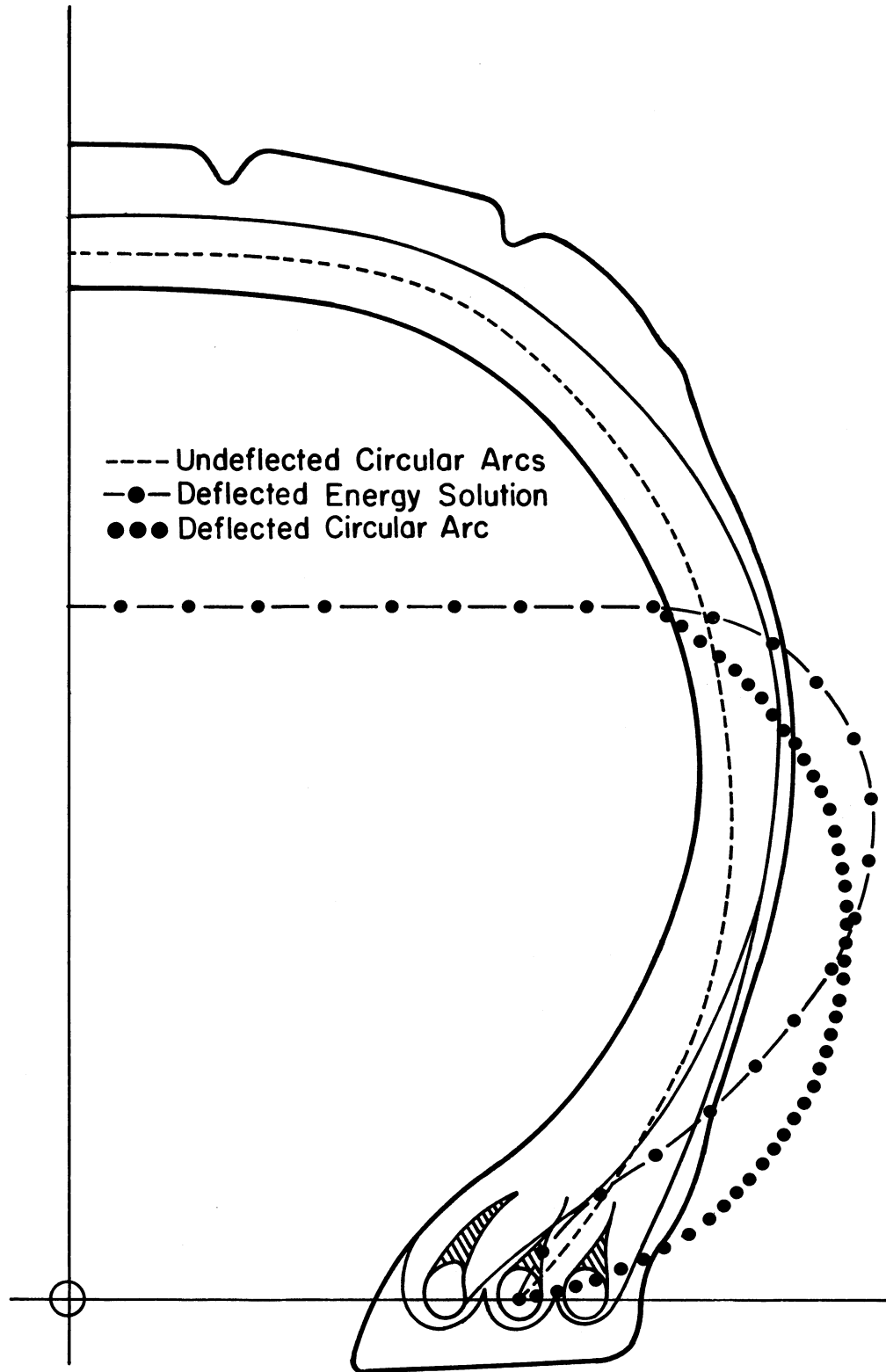


Fig. B2. Deflected and undeflected profiles for 40 x 14 tire

shoulder to the bead, S_L , are known. All of these geometric properties can be measured from appropriate tire cross-section profiles. The location of the shoulder is somewhat arbitrary. However, for this analysis x_c was taken to be 0.75 of the section half-width w , and y_c to be the intersection of $x=x_c$ and the carcass centerline.

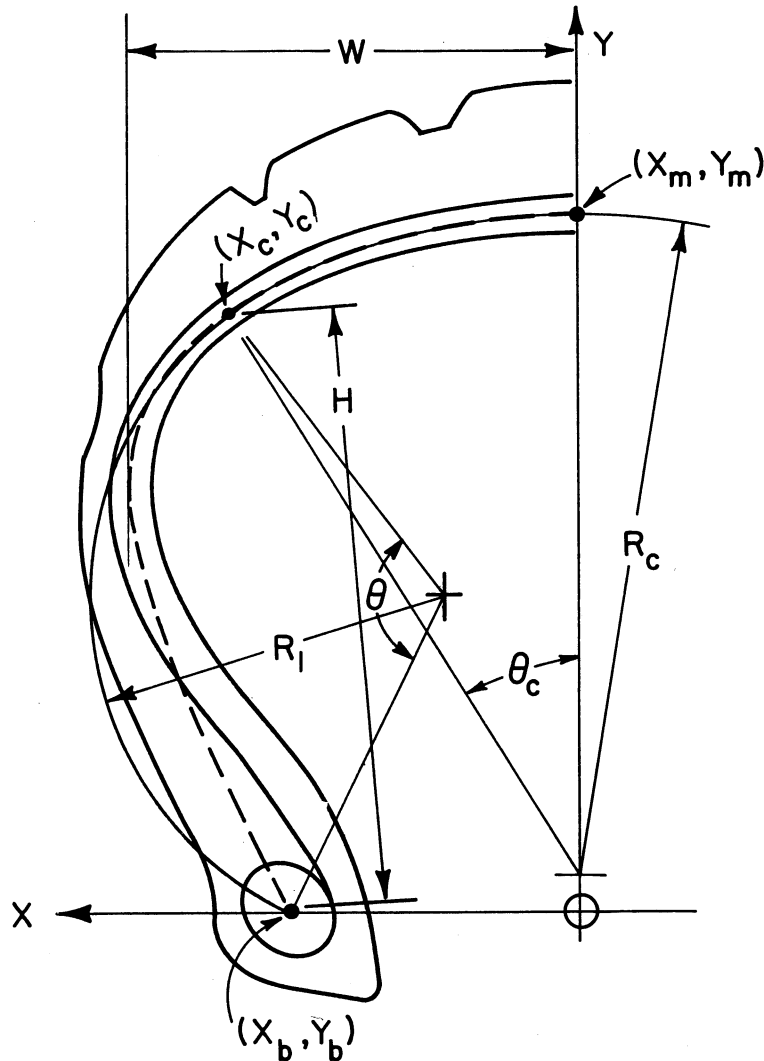


Fig. B3. Tire cross-section illustrating idealized curvatures R_c and R_1

From geometry:

$$R_c = \frac{x_c^2 + (y_c - y_m)^2}{2(y_m - y_c)} \quad (B1)$$

$$\theta_c = \sin^{-1} \left(\frac{x_c}{R_c} \right) \quad (B2)$$

$$S_c = R_c \cdot \theta_c \quad (B3)$$

To find the radius of curvature of the undeflected sidewall one must first determine H:

$$H = \sqrt{(x_c - x_B)^2 + (y_c - y_B)^2} \quad (B4)$$

Noting that $R_1 = S_L / \theta$ and that $H/2 = R_1 \sin(\frac{\theta}{2})$, the angle θ can be found from:

$$\theta - \frac{2S_L}{H} \sin\left(\frac{\theta}{2}\right) = 0 \quad (B5)$$

Solving (B5) for θ then allows the calculation of R_1 .

To calculate the radius of the deflected sidewall it is first assumed that the deflection is greater than $y_m - y_c$ and that the carcass changes from a circular arc of R_c to a flat surface of half-length S_c . It is thus assumed that the x-coordinate of the shoulder in the deflected position is S_c and the y-coordinate is $(y_m - \Delta)$. With the new coordinates of x_c and y_c a new H can be calculated from (B4). Also from the figure:

$$R_f \sin\left(\frac{\theta_f}{2}\right) = \frac{H_f}{2} \quad (B6)$$

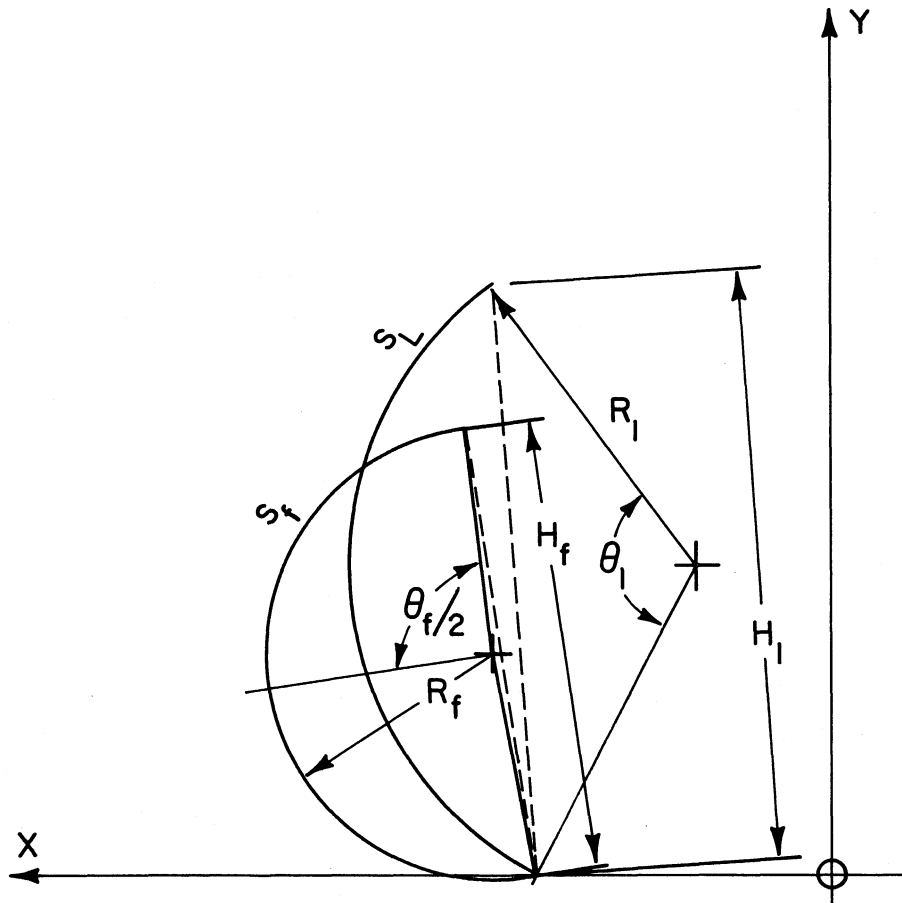


Fig. B4. Geometry of original and final idealized curvatures

$$\theta_f = \frac{S_L}{R_f} \quad (B7)$$

Substituting from (B7) into (B6):

$$R_f \sin\left(\frac{S_L}{2R_f}\right) - \frac{H_f}{2} = 0 \quad (B8)$$

The solution of this transcendental equation for R_f gives the radius of curvature of the deflected sidewall.

APPENDIX C

Bead Tension Analysis

Consider the sidewall of an aircraft tire as shown in fig. C1, first in the undeformed and then in the deformed state.

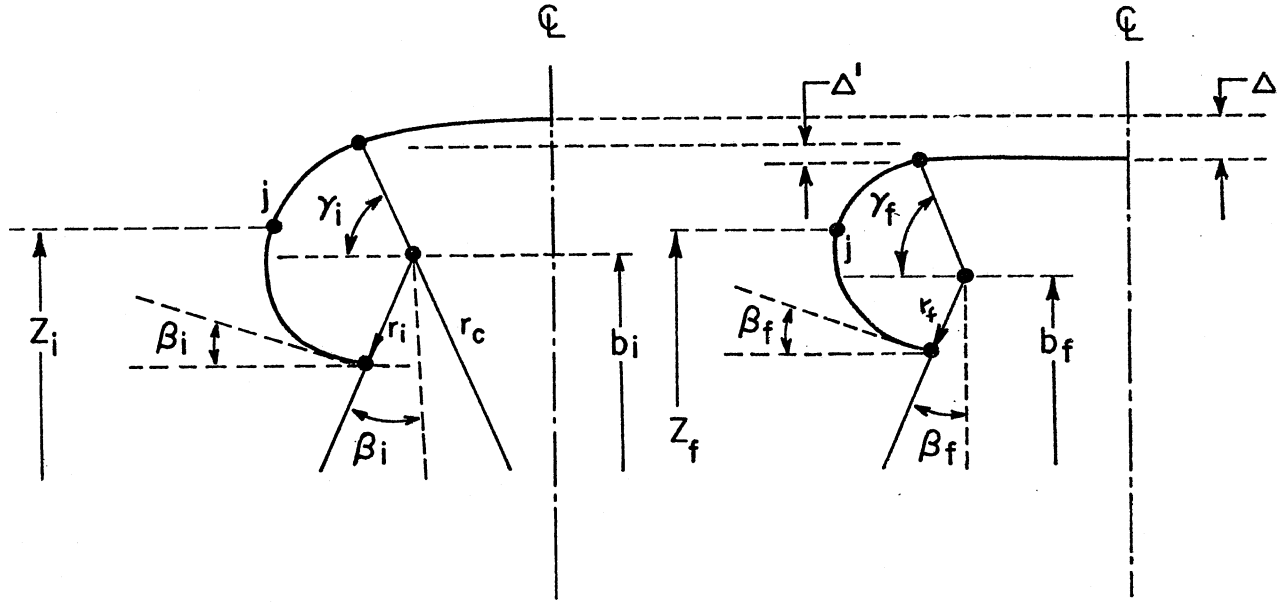


Fig. C1. Sidewall geometry used in bead tension analysis

The membrane forces in the ϕ direction are given by Eq. (2) as

$$(N_{\phi})_B = \frac{P_O}{2} \frac{(z_b^2 - b_i^2)}{z_b \sin \beta_i}$$

$$(N_{\phi})_B = \frac{P_O}{2} \frac{(z_b^2 - b_f^2)}{z_b \sin \beta_f}$$

The angles β are obtained from the tire geometry analysis.

Bead tension may be split into radial and axial components as in fig. C2. The axial component T_z is carried by the wheel flange. The radial component causes bead tension in the amount

$$T_R = (N_\phi \sin\beta) z_b \quad (C4)$$

using a uniformly loaded ring as a model of the bead.

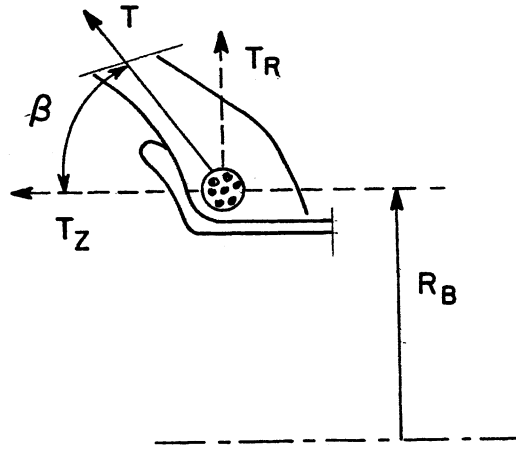


Fig. C2. Details of bead area

Denote the gross area of the bead wires as A_B , and the modulus of the bead bundle based on this gross area as E_B . Then the strain energy stored during one half cycle is

$$U_V = \frac{1}{2} (T_{R_f} - T_{R_i})^2 / (A_B^2 E_B)$$

APPENDIX D

Sidewall Membrane Shear

The membrane forces N_ϕ and N_θ vary as the tire rolls through the contact patch. The variation in N_θ causes a shear stress to be required for equilibrium purposes. This shear stress gives rise to an energy storage, hysteretic loss and heat generation process which is similar to those found by other mechanisms.

Consider the tire cut at its centerline and spread out flat as shown in fig. D1. Equilibrium of forces requires the existence of a membrane shear force N_{xy} as shown. This is caused by the variation in N_θ with circumferential position.

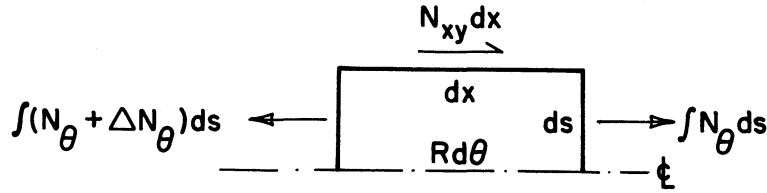


Fig. D1. Idealized view of tire section

Next consider the relation between N_θ and N_ϕ . For a net structure in which loads are carried by the cords alone, Fig. D2 illustrates the division of cord load between N_ϕ and N_θ . If T represents a typical cord load, it may be shown that

$$\frac{N_\phi}{N_\theta} = \tan^2 \alpha \quad N_\theta = N_\phi \cot^2 \alpha \quad (D1)$$

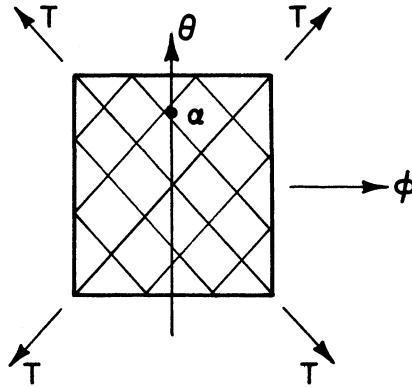


Fig. D2. Idealized net structure

Since N_ϕ is calculated as part of the contribution to strain energy in the sidewall regions I and III, then it is available for computation of N_θ . At any location the variation of N_θ follows the variation of N_ϕ , which is approximately of the form shown in fig. D3.

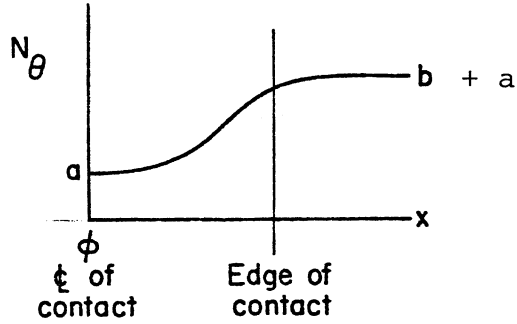


Fig. D3. Variation of N_θ with circumferential position

Letting the variation of N_θ with respect to circumferential position x be approximated by

$$N_\theta = a + b(1 - e^{-c^2 x^2}) \quad (D2)$$

where

$$a = (N_\phi)_B \cot^2 \alpha \quad b = [(N_\phi)_A - (N_\phi)_B] \cot^2 \alpha$$

and $c^2 = \text{constant to be determined later.}$

Since the maximum value of N_{xy} depends on the maximum gradient of N_θ , then it can be determined by differentiation of Equation D2.

$$\frac{dN_\theta}{dx} = 2bc^2 x e^{-c^2 x^2}$$

$$\frac{d^2 N_\theta}{dx^2} = 2bc^2 [1 - 2c^2 x^2] e^{-c^2 x^2}$$

The maximum of $\frac{dN_\theta}{dx}$ occurs at $x = \frac{1}{c\sqrt{2}}$

and results in

$$\begin{aligned} \left(\frac{dN_{\theta}}{dx}\right)_{\max} &= 2b \frac{c^2}{c\sqrt{2}} e^{-\frac{1}{2}} = 0.858 bc \\ &= 0.858c[(N_{\theta})_A - (N_{\theta})_B] \cot^2 \alpha \end{aligned} \quad (D3)$$

From plane equilibrium,

$$\frac{dN_{\theta}}{dx} = \frac{dN_{xy}}{dy} \quad (D4)$$

so that

$$dN_{xy} = 0.858c[(N_{\phi})_A - (N_{\phi})_B] \cot^2 \alpha \cdot dy, \text{ where } y$$

is measured along the circumference of the tire meridian. $\cot \alpha$ varies with this position, so that the net value of N_{xy} at any computational cell is given by

$$N_{xy} = 0.858c[(N_{\phi})_A - (N_{\phi})_B] \int^i \cot^2 \alpha \cdot dy \quad (D5)$$

We now approximate the constant c representing the characteristic distance needed for change in the tensile forces in the circumferential direction, assuming that

$$c \simeq (\text{one contact patch length})^{-1}$$

Since the contact patch length is a function of the tire size and tire deflection, a separate analysis of it is carried out in Appendix F, where it is shown that

$$\text{contact patch length} \simeq [3\Delta(D-\Delta)]^{\frac{1}{2}}$$

where Δ = tire deflection

D = tire diameter

From this the strain energy can be formed

$$U = \frac{1}{2} N_{xy}^2 / h^2 G_{xy} \quad (D6)$$

APPENDIX E

Aircraft tire construction is entirely bias ply and the ply angle range is limited between 30° and 60° for half angles α as illustrated in fig. 7. Previous studies by the authors [ref. 2] and by Walter [3] have shown that within this range of angles the tensile stiffness of the composite bias ply structure can be represented by a simplified analytical model using cords which are inextensible but which are encased in an elastic matrix. This is often given the name "net theory".

One of the shortcomings of such a theory is that some of the other elastic constants needed for this analysis are not predicted well by use of net theory. In an effort to improve the accuracy of those computations a somewhat more advanced theory was constructed around the general framework of a net analysis. In this theory, however, the cord is now assumed to have a certain amount of extensibility so that in extreme cases the stiffness characteristics will not approach indefinitely large values such as is possible with a pure net theory.

Coordinate directions and cord angles are given in fig. E1.

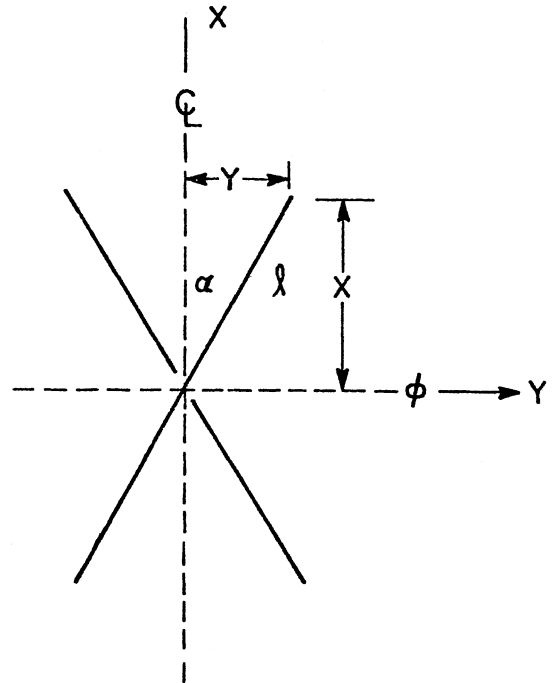


Fig. E1. Detail of idealized bias net structure

Let α = cord half angle with respect to θ , and let

$$\phi = \frac{V_c E_c (1 - V_c)}{2G} = \text{Stiffening Parameter}$$

where

V_c = volume fraction of cord

E_c = cord modulus

G = rubber modulus

Then

$$\lambda = \frac{(\tan^2 \alpha + 1)(2 \tan^2 \alpha - 1)}{2(\tan^2 \alpha + 1)^2 + \phi} \quad \text{and the composite} \quad (E1)$$

elastic modulus in the ϕ direction is found from

$$\begin{aligned} \frac{E_\phi (1 - v_c)}{2G} = & \left[\frac{3}{2} \left\{ (1 + \tan^2 \alpha)^2 + 2\lambda (1 - \tan^4 \alpha) \right. \right. \\ & \left. \left. + \lambda^2 (1 + \tan^2 \alpha)^2 \right\} + \frac{1}{2} (1 - \lambda)^2 (1 + \tan^2 \alpha)^2 \right] \\ & + \lambda^2 \phi \end{aligned} \quad (E2)$$

The Poisson's ratio is

$$\mu_{\theta\phi} = (1 + \tan^2 \alpha)(1 - \lambda) - 1 \quad (E3)$$

The angle distribution in a bias ply aircraft tire is given by

$$\cos \alpha = \frac{r}{r_o} \cos \alpha_o$$

where

α_o = crown angle

r_o = crown radius

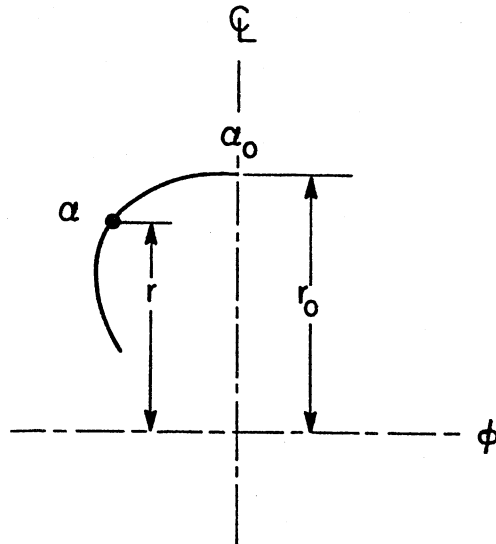


Fig. E2. Tire cross section

APPENDIX F

Referring to fig. F1, the length of the contact may be approximated as follows

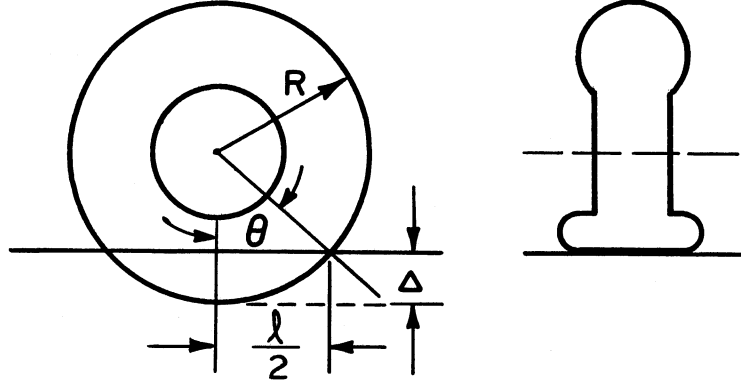


Fig. F1. Idealized geometry

From geometry,

$$R(1 - \cos \theta) = \Delta$$

$$\cos \theta = 1 - \frac{\Delta}{R} \quad \sin^2 \theta = \frac{2\Delta}{R} - \frac{\Delta^2}{R^2}$$

$$\frac{\ell}{2} = R \sin \theta \quad \ell^2 = 4R^2 \left(\frac{2\Delta}{R} - \frac{\Delta^2}{R^2} \right) \approx 4\Delta(D - \Delta)$$

From reference 5, the empirical expression for the contact patch length L is given as 0.85 times the geometric intersection length ℓ , so that

$$L^2 = (0.85)^2 \times 4 (D - \Delta) \approx 3\Delta(D - \Delta)$$

from which

$$L = \sqrt{3\Delta(D - \Delta)}$$

APPENDIX G

Independent of other effects, the tire cycles between zero tread compressive stress and a maximum compressive stress.

Measurements indicate a maximum pressure/unit length at the centerline of contact, approximating 1.25 x average inflation pressure x width.

Examine three possible pressure distributions, all giving rise to the same load/unit length. See Fig. G-1.

$$\text{Stored energy} \sim \frac{p^2}{E} \sim \int_{-w/2}^{w/2} p^2 dy \quad \text{assuming } E = \text{constant across the tread.}$$

$$(a) \quad E_a = \int_0^w (1.25p_o)^2 dy = 1.5625p_o^2 w \quad \text{for constant pressure} \quad (G1)$$

$$(b) \quad \text{Parabola 1; } p = p_m \left[1 - \left(\frac{2y}{w}\right)^2\right]$$

$$E_b = \int_{-w/2}^{w/2} p^2 dy = p_m^2 \left\{ y - \frac{8y^3}{3w^2} + \frac{16y^5}{5w^4} \right\} \Big|_{-w/2}^{w/2} = p_m^2 \cdot \frac{8}{15} w \quad (G2)$$

$$\text{But } \int_{-w/2}^{w/2} p dy = 1.25 p_o w = \int_{-w/2}^{w/2} p_m \left[1 - \frac{4y^2}{w^2}\right] dy = \frac{2p_m w}{3}$$

$$\therefore p_m = \frac{3}{2} \times 1.25 p_o \quad (G3)$$

$$\therefore E_b = p_m^2 \times \frac{8}{15} w = \frac{9}{4} \times \frac{25}{16} p_o^2 \times \frac{8}{15} w = 1.875 p_o^2 w = 1.2 \times E_a \quad (G4)$$

(c) Parabola 2: $p = p_m \left(\frac{4y^2}{w^2} \right)$

$$\int_{-w/2}^{w/2} p dy = 1.25 p_o w = p_m \int_{-w/2}^{w/2} \frac{4y^2}{w^2} dy = p_m \left. \frac{4y^3}{3w^2} \right|_{-w/2}^{w/2}$$

$$E_c = \int p^2 dy = p_m^2 \int \frac{16y^4}{w^4} dy = p_m^2 \frac{w}{5} = 2.8125 p_o^2 w = 1.80 E_a$$

We adopt a conservative value of $\frac{1.80+1.20}{2} = 1.5 \times \underline{\text{uniform}}$ case. Assume uniform contact pressure of $1.25 \times p_o$. Then multiply by 1.5 factor for shape distribution, giving a total value of $1.25 \times 1.50 p_o = 1.875 p_o$.

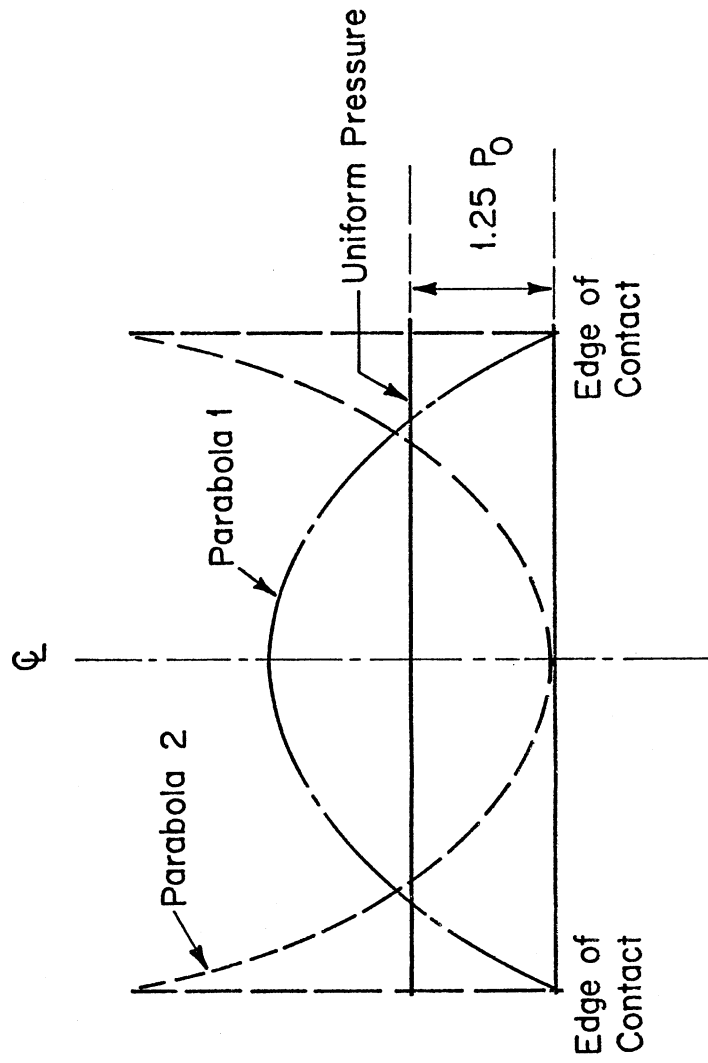


Fig. G1. Transverse pressure distributions

APPENDIX H

Thermal Analysis

In the thermal analysis, account is taken of conduction to neighboring elements, conduction to the road surface, convection to the outside air and to the inside air, and heat generation within each element. In writing the heat balance equation for each element it is necessary to provide effective heat transfer and heat generation coefficients for each element. The necessary coefficients are:

$$AV, AH = \frac{K_R \cdot a \cdot \Delta t}{C_R \cdot \rho_R \cdot v \cdot d}$$

$$QB = \frac{\dot{q} \cdot v \cdot \Delta t}{C_R \cdot \rho_R \cdot v}$$

$$HR = \frac{1}{\frac{1}{\frac{K_R \cdot a}{C_R \cdot \rho_R \cdot v \cdot d}} + \frac{1}{\frac{h_R \cdot a}{C_R \cdot \rho_R \cdot v}}}$$

$$HA = \frac{1}{\frac{1}{\frac{K_R \cdot a}{C_R \cdot \rho_R \cdot v \cdot d}} + \frac{1}{\frac{h_A \cdot R_i \cdot a}{C_R \cdot \rho_R \cdot v \cdot R_1}}}$$

$$HC = \frac{1}{\frac{1}{\frac{K_R \cdot a}{C_R \cdot \rho_R \cdot v \cdot d}} + \frac{1}{\frac{h_c \cdot a}{C_R \cdot \rho_R \cdot v}}}$$

$$HF = \frac{1}{\frac{1}{\frac{K_R \cdot a}{C_R \rho_R \cdot v \cdot d}} + \frac{1}{\frac{K_A \cdot a}{C_A \rho_A \cdot v d}} + \frac{1}{\frac{h_f \cdot a}{C_R \rho_R \cdot v}}}$$

where:

- AV, AH - effective heat conduction coefficeints, neighboring elements
- QB - effective heat generation coefficient, each element
- HF - effective heat transfer coefficient, tire-rim interface
- HR - effective heat transfer coefficient, tire-road interface
- HA - effective heat transfer coefficient, tire-outside air interface
- HC - effective heat transfer coefficient, tire-contained air interface
- v = volume of each element
- a = area across which heat is transferred
- d = distance between nodes
- Δt = time increment - selected
- \dot{q} = rate of heat generation each element - see earlier sections.
- K_R = thermal conductivity of rubber = 5×10^{-4} cal·cm/°C·cm²·sec
- K_A = thermal conductivity of rim = .48 cal·cm/°C·cm²·sec
- C_R = specific heat of rubber = 0.5 cal/gm °C
- C_A = specific heat of rim = .23 cal/gm °C
- ρ_R = density of rubber = 1 gm/cm³
- ρ_A = density of rim = 2.7 gm/cm³
- h_R = film heat transfer coefficient, tire-road interface
= .25 cal/°C·cm²·sec
- h_A = film heat transfer coefficient, tire-outside air interface
= $(1.3 \times 10^{-4} + 4 \times 10^{-7} V(\text{cm/sec}))$ cal/°C·cm²·sec
- h_c = film heat transfer coefficient, tire-contained air interface
= 1×10^{-4} cal/°C·cm²·sec
- h_f = film heat transfer coefficient, tire-rim interface
= .5 cal/°C cm²·sec

Typical heat balance equations for the individual elements of the 22x5.5 8PR tire are listed below where each equation has been solved for the change in temperature which takes place during a given increment of time.

The inside elements all have an equation of the form:

$$\begin{aligned}\Delta T_{I,1} = & QB(I,1) + AH(I,1)(T_{I,2} - T_{I,1}) + AV(I,1)(T_{I+1,1} - T_{I,1}) \\ & + AV(I-1,1)(T_{I-1,1} - T_{I,1}) + HC(I)(TC - T_{I,1})\end{aligned}$$

The middle elements all have an equation of the form:

$$\begin{aligned}\Delta T_{I,2} = & QB(I,2) + AH(I,2)(T_{I,3} - T_{I,2}) + AH(I,1)(T_{I,1} - T_{I,2}) \\ & + AV(I,2)(T_{I+1,2} - T_{I,2}) + AV(I-1,2)(T_{I-1,2} - T_{I,2})\end{aligned}$$

The outside elements not in contact with the road surface or rim have an equation of the form:

$$\begin{aligned}\Delta T_{I,3} = & QB(I,3) + AH(I,2)(T_{I,2} - T_{I,3}) + AV(I,3)(T_{I+1,3} - T_{I,3}) \\ & + AV(I-1,3)(T_{I-1,3} - T_{I,3}) + HA(I)(TA - T_{I,3})\end{aligned}$$

The outside elements in contact with the rim have the same form except HA is replaced by HF and TA by TF.

The outside elements in the tread region are assumed to be in contact with the air 90% of the time and in contact with the road surface 10% of the time. The heat balance equation for these elements is of the form:

$$\begin{aligned}\Delta T_{I,3} = & QB(I,3) + AH(I,2)(T_{I,2} - T_{I,3}) + AV(I,3)(T_{I+1,3} - T_{I,3}) \\ & + AV(I-1,3)(T_{I-1,3} - T_{I,3}) + 0.9 HA(I)(TA - T_{I,3}) \\ & + 0.1 HR(I)(TR - T_{I,3})\end{aligned}$$

In this analysis the outside air temperature T_A , the rim temperature T_F , and the road surface temperature T_R are assumed to remain constant. However, the change in the contained air temperature T_C is approximated as follows:

$$T_C = \frac{h_c \cdot A \cdot \Delta t \cdot (T_i - T_C)}{C_c \rho_c \cdot V}$$

where:

$$C_c = .24 \text{ cal/gm}^\circ \text{ c}$$

$$\rho_c = .0013 \text{ gm/cm}^3$$

$$T_i = \text{weighted average of inside surface temperatures}$$

For the 22x5.5 8PR tire analyzed, the approximate values of A and V are 30.4 cm^2 and 90.35 cm^3 , respectively. Thus, for this tire:

$$\Delta T_C = .1078 (\bar{T}_i - T_C) \cdot \Delta t$$

APPENDIX I

Contained Air Temperature

Consider the tire cross-section as shown in fig. I1. Let θ be the area weighted average of the temperatures on the inner surface of the tire over the region 0-1-2. Let y be the contained air temperature. Then the equation for temperature rise of the contained air is

$$c_p \cdot \rho \cdot V \frac{dy}{dt} = hA(\theta - y) \quad (I1)$$

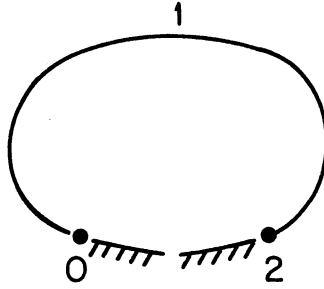


Fig. I1. Tire cross-section

where

h = average heat transfer coefficient

A = surface area of convection 0-1-2

c_p = specific heat of air

ρ = air density

V = volume of contained air

Let $hA/c_p \rho V = \beta$. Then equation I1 becomes

$$\frac{dy}{dt} + \beta y = \beta \theta \quad (I2)$$

In the initial stages of tire heating the tire inner surface temperatures rise almost linearly, so that $\theta = c \times t$ where c is a constant. In this case equation (I2) has a solution

equation (I2) has a solution

$$y = \theta - \frac{c}{\beta}(1-e^{-\beta t}) \quad (I3)$$

This solution lags behind the tire inner surface temperature.

For longer times when θ is determined numerically, the contained air temperature y must be calculated by the methods previously described using a finite difference form of equation (I1).

APPENDIX J

Tread Friction

The tread region in contact with the runway can be approximated in a two dimensional sense as an elastic member under the action of both tensile forces and surface friction. This is illustrated in figure J1.

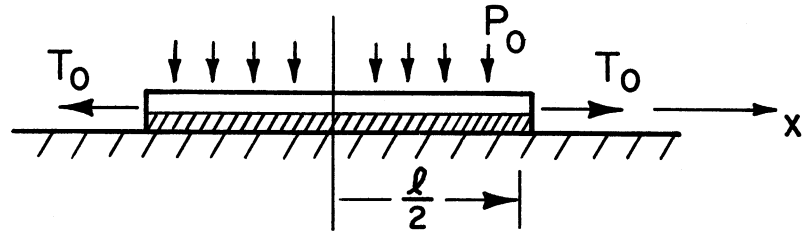


Fig. J1. Idealized section of tire tread with runway

Let u = displacement in x direction

Let the tension $T = AE \frac{\partial v}{\partial x}$

where A = cross-sectional area

E = modulus of elasticity

Let K = shear stiffness of the tread rubber, which is assumed not to slip on the runway.

The equation governing deformation is

$$\frac{d^2 u}{dx^2} - \frac{K}{AE} u = 0 \quad (J1)$$

whose solution is

$$u = C_1 e^{\lambda x} + C_2 e^{-\lambda x} \quad (J2)$$

where

$$\lambda = \sqrt{\frac{K}{AE}}$$

Using the boundary condition

$$(AE \frac{\partial v}{\partial x})_{x=\frac{l}{2}} = T_0$$

One obtains

$$T(x) = \frac{T_o}{\sqrt{KA\epsilon}} \cdot \frac{(e^{\lambda x} + e^{-\lambda x})}{(e^{\lambda \ell/2} + e^{-\lambda \ell/2})} \quad (J 3)$$

This expression may be used to estimate the tension in the tread across the width of the contact patch. The value of K can be estimated from the known thickness, modulus and shear stiffness of the tread. In general the tread tension is reduced across the width of contact.

1. Report No. NASA CR-3629		2. Government Accession No.		3. Recipient's Catalog No.	
4. Title and Subtitle HEAT GENERATION IN AIRCRAFT TIRES UNDER FREE ROLLING CONDITIONS				5. Report Date October 1982	
				6. Performing Organization Code	
7. Author(s) Samuel K. Clark and Richard N. Dodge				8. Performing Organization Report No.	
9. Performing Organization Name and Address University of Michigan Department of Mechanical Engineering Ann Arbor, MI 48109				10. Work Unit No.	
				11. Contract or Grant No. NSG-1607	
12. Sponsoring Agency Name and Address National Aeronautics and Space Administration Washington, DC 20546				13. Type of Report and Period Covered Contractor Report	
				14. Sponsoring Agency Code	
15. Supplementary Notes Langley technical monitor: John L. McCarty					
16. Abstract A method has been developed for calculating the internal temperature distribution in an aircraft tire while free rolling under load. The method uses an approximate stress analysis of each point in the tire as it rolls through the contact patch, and from this stress change the mechanical work done on each volume element may be obtained and converted into a heat release rate through a knowledge of material characteristics. The tire cross-section is then considered as a body with internal heat generation, and the diffusion equation is solved numerically with appropriate boundary conditions of the wheel and runway surface. Comparison with data obtained with buried thermocouples in tires shows good agreement.					
17. Key Words (Suggested by Author(s)) Aircraft tires Tire heating Tire thermal analysis			18. Distribution Statement Unclassified - Unlimited Subject Category 03		
19. Security Classif. (of this report) Unclassified	20. Security Classif. (of this page) Unclassified	21. No. of Pages 98	22. Price* A05		